UNIVERSIDAD DE CHILE
FACULTAD DE CIENCIAS FÍSICAS Y MATEMÁTICAS
DEPARTAMENTO DE INGENIERÍA MECÁNICA

CONSIDERING A TEMPERATURE GRADIENT NEAR THE PIN FOR A FRICTION STIR WELDING (FSW) THERMOPHYSICAL MODEL USING SCALING ANALYSIS

TESIS PARA OPTAR AL GRADO DE
MAGÍSTER EN CIENCIAS DE LA INGENIERÍA, MENCIÓN MECÁNICA

MEMORIA PARA OPTAR AL TÍTULO DE
INGENIERO CIVIL MECÁNICO

DIEGO IGNACIO ROJAS MUÑOZ

PROFESOR GUÍA:
RUBÉN FERNANDEZ URRUTIA

PROFESOR CO-GUÍA:
PATRICIO MENDEZ PINTO

COMISIÓN:
ALI AKBARIFAKHRABADI

Este trabajo ha sido parcialmente financiado por el Gobierno de Canadá a través de la beca "Emerging Leaders in the Americas" (ELAP)

SANTIAGO DE CHILE
2022

RESUMEN DE LA TESIS PARA OPTAR
AL GRADO DE MAGÍSTER EN CIENCIAS
DE LA INGENIERÍA, MENCIÓN MECÁNICA
RESUMEN DE LA MEMORIA PARA OPTAR
AL TÍTULO DE INGENIERO CIVIL MECÁNICO
POR: DIEGO IGNACIO ROJAS MUÑOZ
FECHA: 2022
PROF. GUÍA: RUBÉN FERNANDEZ

MODELO TERMOFÍSICO PARA SOLDADURA POR FRICCIÓN Y AGITACIÓN UTILIZANDO ANÁLISIS DE ESCALA CONSIDERANDO UN GRADIENTE DE TEMPERATURA CERCA DEL PIN

La soldadura por fricción y agitación (FSW) es un proceso de soldadura en estado sólido. Se caracteriza por su capacidad de soldar materiales que son considerados no soldables y por las excelentes propiedades mecánicas de la unión. Actualmente, las aplicaciones de FSW están limitadas a un nicho de ciertos tipos de aleaciones y rangos de espesores. Dichas aplicaciones incluyen principalmente soldadura especializada de aluminio en barcos, cohetes, trenes y aviones, mas no en el área nuclear (debido a los espesores y materiales), petróleo y gas, minería u otros. Un obstáculo para ampliar las aplicaciones de FSW es el debate que aún existe en torno a la física involucrada en el proceso, por lo que no existen reglas de diseño para la selección de parámetros del proceso. Este trabajo busca llenar parte del vacío teórico y ofrecer una manera de predecir una correcta soldadura. Una iteración del modelo de Mendez *et al.* es presentada. El modelo considera transferencia de calor y deformación plástica del material durante el proceso y usa el análisis de escala para resolver algunas de las ecuaciones. En esta iteración, un gradiente de temperatura cerca del pin es considerado para tomar en cuenta las pérdidas de calor por la herramienta. Estimaciones de máxima temperatura y torque se comparan con resultados teóricos y numéricos de la literatura. Un total de 280 valores de diferentes materiales incluyendo aleaciones de aluminio, magnesio, titanio y aceros al carbono son puestos a prueba. Las estimaciones capturan valores correctos cercanos a los reportados. La máxima temperatura fue subestimada por cerca del 7% y el torque entre un 9% y un 14%.

RESUMEN DE LA TESIS PARA OPTAR
AL GRADO DE MAGÍSTER EN CIENCIAS
DE LA INGENIERÍA, MENCIÓN MECÁNICA
RESUMEN DE LA MEMORIA PARA OPTAR
AL TÍTULO DE INGENIERO CIVIL MECÁNICO
POR: DIEGO IGNACIO ROJAS MUÑOZ
FECHA: 2022
PROF. GUÍA: RUBÉN FERNANDEZ

CONSIDERING A TEMPERATURE GRADIENT NEAR THE PIN FOR A FRICTION STIR WELDING (FSW) THERMOPHYSICAL MODEL USING SCALING ANALYSIS

Friction stir welding (FSW) is a solid-state joining process. It is noted for welding materials that are considered unweldable by other welding processes and for achieving joints with excellent mechanical properties. Currently, the applications of this process are limited to niche applications in a relatively narrow range of alloys and thicknesses. Applications include mostly aluminum welding in specialized ships, rockets, high-speed trains, and airplanes, but do not yet include nuclear (too high thickness and ferrous materials), oil and gas, mining, and more. One of the bottlenecks to a broader applicability of FSW is that there is still debate about the physics involved in it, resulting in no engineering design rules for selecting process parameters. This work aims to fill part of that theoretical void and to offer a way of predicting successful welds. An iteration of a model by Mendez *et al.* is presented. The model considers heat transfer and plastic deformation of the material during a FSW process and uses scaling analysis to help solve some of the complex equations. In this iteration, a temperature gradient near the pin is considered to take into account heat losses through the tool. Estimations of maximum temperature and torque are compared against experimental and numerical results in the literature. A total of 280 values of different materials including aluminum alloys, magnesium alloys, titanium alloys and steels are tested. The estimations captured correct values, close to the ones reported in the literature. The maximum temperature was underpredicted by approximately 7% and torque was underpredicted by approximately 9% to 14%.

To my parents. Thank you for your support and sacrifice.

Acknowledgments

I would like to thank Professor Patricio Mendez, for the opportunity that he gave me, to travel and work alongside him and other remarkable people. For motivating me to go one step further, for always being there when I needed and for always worrying about our well-being.

I would also like to thank my friends. For being there every step of the way. Thanks to Juan Pablo Achondo and Juan Pablo Messina for being like my brothers all these years. Thanks to Javiera Miravalles for always being there, encouraging and motivating me to continue when this process seemed endless. Thanks to Camila Aguilar, Benjamín Easton, Diego Bustamante and Alain Authievre for being incredible friends and giving me some of the best moments during these years. Thanks to Felipe Saavedra and Yerin Saavedra for being present since my first year of university. And finally, thanks to the amazing group of latinos in Canada. Those months were as good as they could be thanks to all of you.

I would also like to thank my family, for their support all this time. Thanks to my aunt and cousins for always keeping an eye on me. Thanks to my grandmother for always taking care of me and giving me a meal on those long study sessions. To my brothers Pablo and Rodrigo for being my mentors and my best friends. For those who are not longer with us, you too were an important part of this.

Finally, I would like to especially thank my parents Jorge and Marisa for supporting me all the way through school and university. For standing by me when things went wrong and for celebrating my achievements. For giving me the tools and opportunities for me to be where I am and the sacrifices they had to do for that. Without them this could not have been possible.

Table of Content

List of Tables

List of Figures

Chapter 1

Introduction

1.1 Friction Stir Welding

Friction stir welding (FSW) is a solid-state joining process that differs from other welding processes by commonly not melting the work-piece. It was invented at The Welding Institute (TWI) in the UK in 1991 [3] and has a series of advantages over other welding techniques. As the energy consumption is between 2% and 5% of the energy consumed by an arc-based welding process, FSW is considered a green process. In addition, friction stir welding has proven to be viable joining magnesium-, ferrous- and titanium-based alloys, dissimilar alloys and even dissimilar materials, even though research and industrial attention was originally around aluminum alloys. [4] Such potential has not been ignored, as a variety of industrial applications can be found: Ford Motor Company used FSW in the centre tunnel of the Ford GT sportscar [5], Boeing Company used FSW to weld the Delta II and Delta IV launch vehicles fuel tank [6] and Nichols Brothers Boat Builders used FSW to build all the flight decking and underbelly structure of the Sea Fighter (FSF-1) combat ship. [7]

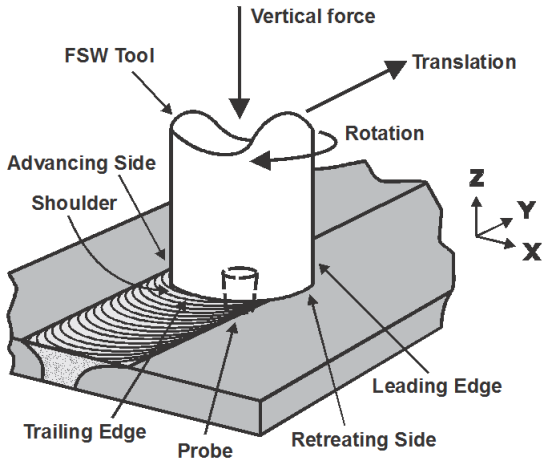

Figure 1.1: Schematic diagram of friction stir welding. [1]

The process consists of a non-consumable tool rotating with a perpendicular axis to the base plates. The tool penetrates the plates and deforms them through heat generated by friction and plastic deformation so that both independent pieces are locally mixed and joined, as Figure 1.1 shows. Such tool consists of a shoulder and a pin or probe where the shoulder has a diameter around three times the diameter of the pin, and the length of the pin is marginally shorter than the thickness of the plate being welded. The plates are usually welded in a butt joint configuration, although lap joints are also common for this type of process. Additionally, most of the testing for FSW is done using a common milling machine, yet there are companies as Hitachi and Fooke that offer machines specifically for FSW.

Because melting does not occur during the joining process, FSW generates pieces with excellent mechanical properties and avoids the possibility of common defects as segregation, dendritic structure and hot cracking or porosity formation associated with fusion-based welding techniques. Furthermore, key features of the weld depend on different welding parameters. [4] The main parameters are the rotation speed and travel speed of the tool as well as the size of tool used in the process. These parameters will determine the microstructure of the material in the welded section of the piece mainly because of the temperature reached during the process. Other relevant factors to consider are the material being welded, the thickness of the plate and the type of tool being used as well as the forces between the tool and the work-piece.

Research on FSW is extensive and diverse. Experimental tests are usually conducted to see how the parameters or the so called "independent variables" [8] affect the temperature fields during the process, the torque and forces experimented by the tool and ultimately, the quality of the weld. Other similar tests involve checking the hardness and strength of the joint, comparing different materials and joining dissimilar materials. However, not all research is done upon testing. Simulations using computational fluid dynamics (CFD) and finite element methods have proven to be successful representing a FSW process. Considering that this is a complex process, involving many coupled physical phenomena occurring at the same time [9], when compared with experimental results, simulations have proven to be reliable.

Additionally, mathematical models made to predict certain critical values such as peak temperature, emerged. In this kind of research, most of the physical phenomena are accounted for or estimated following the background on the subject. As some of the interactions between the tool and the work-piece remain unknown, usually this models take some assumptions and considers some simplifications. Moreover, is not uncommon for this sort of research to apply some kind of technique to solve complex, often non-linear equations.

1.2 Objectives

1.2.1 General Objective

The main objective of this work is to establish new equations for the Mendez *et al.* [2] coupled model to estimate maximum temperature and torque during a FSW process considering the physical phenomena involved, in particular heat transfer and plastic deformation.

1.2.2 Specific Objectives

To accomplish the main objective, the following specific objectives have to be considered:

- Establish the expressions for a modified coupled model based on the one proposed by Mendez *et al.* [2]
- Generate an updated database adding new data to the one used in Mendez *et al.* [2]
- Evaluate the updated database using the modified model.
- Compare the behavior of the model using different optimization approaches.
- Compare the behavior of torque estimations when shoulder effect is considered.
- Generate correction factors for the results based only on experimental data.
- Analyze the results, in particular data that differs from the trend.

1.3 Scope of the Study

This research solely considers the evaluation of data gathered from a number of publications done on FSW tests using different types of materials, FSW machines and measurement equipment. By no means this study consider any FSW test being done to collect data.

Chapter 2

Literature Review

2.1 FSW Background

As it was mentioned before, research on FSW is not uncommon and can be classified into three different categories: experimental tests, software simulation and mathematical models. Each one will be covered next in this section.

2.1.1 Experimental tests on FSW

This kind of research represent the primary source of knowledge of FSW and it is often used as a reference for simulations and mathematical models. Usually, in this sort of publications authors test the quality of the weld using different rotation and travel speed for a specific material [10–24], compare the behavior of different materials [11, 21, 25], observe the microstructure of the weld [12, 17, 22, 26–33] and perform different mechanical tests on the welds. [14, 22, 24, 29–32]

However, no matter what the focus of the study is, temperature reached during the process is key to understand the properties of the joint. Fehrenbacher *et al.* [34] described the weld zone temperatures as of great interest because it determines the microstructural evolution, and as a result the metallurgical and mechanical properties of the weld. Nandan *et al.* [8] concludes in a FSW review that peak temperature increases with increasing rotational speed and decreases slightly with travel speed. Edwards *et al.* [19] running FSW tests on Ti-6Al-4V states the same, saying that tool rotation speed is the dominant variable on peak temperature generation and that travel speed of the tool has a minimal influence on peak temperature. Additionally, the author made a relationship between grain size and speed parameters declaring that higher rotational speeds lead to larger grains than the lower rotational speeds and that there is a slight decrease in grain size with increasing travel speed.

Microstructure of the joint conditions the mechanical properties of the weld. Materials can be highly susceptible to slight changes produced by different welding parameters. So much so that microstructure on the advancing side of the weld (this is the side of the weld where the direction of the rotation and travel are the same) is different from the retreating side. As Liu *et al.* [35] demonstrated on 6061-T6 aluminum welds, the hardness of particular age-hardened aluminum alloys tends to be lower in the heat-affected zone on the retreating side, which then becomes the location of tensile fracture in cross-weld tests. Lee *et al.* [36] proved that this was also the case for pure titanium.

2.1.2 Simulations on FSW

The complexity of the FSW process represents a challenge when a simulation wants to be made. Large plastic deformation, material flow, mechanical stirring, surface interaction between the tool and the work-piece, dynamic structural evolution and heat generation resulting from friction and plastic deformation are the physical phenomena occurring at the same time during a FSW weld. Therefore, as He *et al.* [9] mentions in a FSW numerical analysis review, FSW models cover a broad range of complexity, from the simple conduction heat transfer models [37], to metal flow models [15] and fully coupled models [38].

Often, simulations are compared with experimental tests to verify the results and they frequently agree. For example, Nandan *et al.* [11,38] performed simulations for stainless steel and aluminum alloy using FLUENT. In the publications, the computed temperature versus time plots and the geometry of the thermomechanically affected zone region agreed well with corresponding independent experimental results. Analogously, Hamilton *et al.* [39] performed welds using aluminum 7136 and developed a simulation using a finite element method model. In this work, the predicted temperature of the simulation agrees with the one reported by other authors using the same material and parameters. Besides, temperature fields show direct correlation with the microstructure of the welds. Finally, the results of the thermal model also suggest pseudo-aging of the supersaturated weld areas that can form a network of strengthening phases in the joint.

2.1.3 Mathematical models on FSW

In an effort to simplify calculations and to obtain reliable estimations of the most relevant values for a given FSW Weld, mathematical models show to be a useful method. Usually, this models depend on assumptions or simplifications to propose equations that are possible to solve. Most of this equations describe heat generation, heat transfer and material flow. It is fairly common for authors to solve, for example heat generation and heat transfer separately to get more approachable solutions. [2, 38, 40–42]

Contact between the tool and the work-piece is key to estimate heat generation. The literature proposes two different approaches: the sliding or sticking condition. On the one hand, sliding condition occurs when the shear stress of the contact between tool and work-piece is smaller than the material yield shear stress. In this case, the material experiences elastic deformation and heat generation is predominantly by friction. On the contrary, if the contact shear stress exceeds the yield shear stress of the material, this will stick to the tool. In such a case, the sticking condition dominates heat generation by plastic deformation of the work-piece. Although debate around heat generation continues between these two perspectives or even a combination of both, sticking condition seems to be the favorite. Schmidt *et al.* [43] delivers an extensive discussion on the calculation of heat generation rates between both conditions. Reynolds, Ulysse and Colgrove *et al.* [14, 16, 44] consider only sticking condition opposing to Nandan *et al.* [8] who, among others [43], consider heat generation from both phenomena and proposes an "extent of slip" factor.

Relevant models to describe material behavior and physical phenomena are often useful to authors. Heat transfer through the work-piece is typically based on Rosenthal's equation. [45, 46] This model is widely used in welding problems as it can represent a moving heat source on a thin plate. Despite the fact that the basic model considers some simplifications as constant material properties and neglected heat losses, it is a powerful resource to calculate heat transfer in the work-piece. On the other hand, Zener-Hollomon constitutive model can be applied to account for the combined effects of temperature and strain rates that a particular material submits during FSW. [8]

In this work, a coupled model of heat transfer and plastic deformation is improved using most of the resources mentioned before, together with scaling analysis to simplify equation resolution.

2.2 Scaling Analysis Background

Scaling analysis is a procedure done to obtain characteristic values for the unknown variables in the governing equations of a problem. A characteristic value is generally considered the maximum order of magnitude of a variable. [47] The procedure consists on neglecting terms in the equations determined by self consistent simplifications. [48] Said self consistency denote that the test of whether the neglected terms are small is made using the estimations which assume those terms are negligible. [49] Mendez [50] states that scaling provides a simple closed-form solution applicable to any system that falls in a range of parameters. Within the benefits of scaling for modeling materials processes, some of these are that it helps to determine the relative importance of the multiple driving forces on a system, it is useful to determine the terms that can be simplified in a particular problem and it is able to produce simpler equations that account for the relevant phenomena.

Scaling a problem can be a tiring process if performed manually. Many systems involve two or more equations and some of them are coupled, making it virtually impossible for them to be solved without using some kind of iterative working software. The main procedure to develop the scaling of a problem, as described in [50], is:

1. Write the governing equations including boundary conditions.
2. Scale dependent, independent and differential equations, considering that some of the characteristic values may be unknown.
3. Replace scaled expressions into governing equations.
4. Normalize governing equations using the term expected to be dominant.
5. Solve for the unknown characteristic values by choosing terms where they are present and making their coefficients equal to 1.
6. Verify that the terms not chosen are smaller than 1.
7. If one or more of the terms is larger than 1, normalize again picking different terms to solve for the unknowns.

2.3 Coupled Model

A coupled model of heat transfer and plastic deformation for FSW is presented to estimate temperature and torque. This work represents a modification done to the one proposed by Mendez *et al.* in [2]. This model describes the heat generation and plastic deformation around the pin using fundamental continuum mechanics equations approximated using scaling analysis and is tested against published models and measurements for a series of different materials. The original model considers heat losses by conduction to the tool by contemplating less than a 100% heat efficiency. This was done in pursue of simplifying the mathematical treatment. This modification for the model addresses the inconsistency between temperature profile and efficiency by accounting properly for the temperature profile in the work-piece. Moreover, improvements to the treatment of the constitutive relationship between strain rate, stress and temperature are considered.

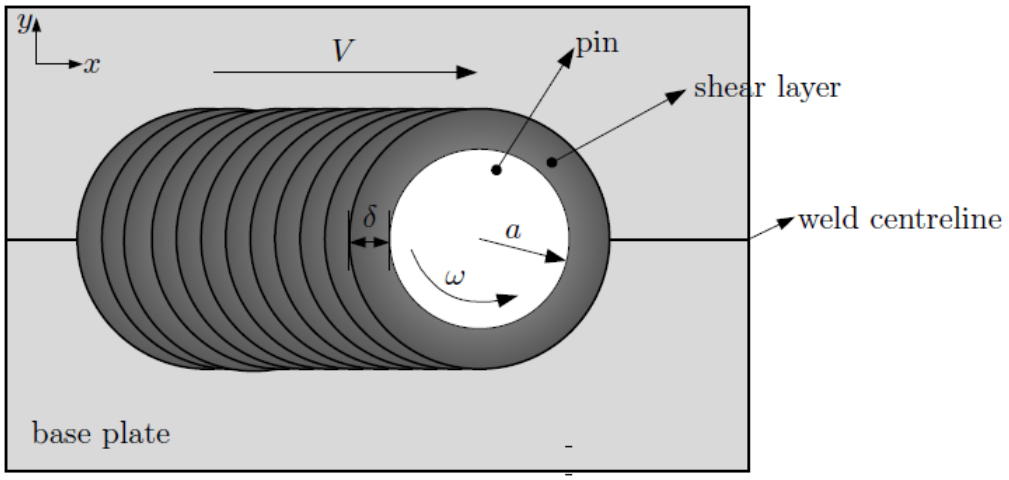

Figure 2.1: Schematic of the work-piece during FSW. Shear layer is represented as no effect of the shoulder is considered.

A schematic view of FSW is presented in Figure 2.1. It is worth noting that no effect of the shoulder is being considered in the representation, which means that the view depicted is from a certain depth under the surface of the plate. On the other hand, the pin is represented as a perfect circle. This means that the shape of the pin is a smooth cylinder, which is a simplification considered in the model as tool pins usually are threaded or have various features and shapes. [4] Furthermore, the pin is surrounded by a ring-shaped figure. This is called the shear layer. This layer is where plastic deformation of the material occurs. Within the length δ of the layer, the material of the work-piece suffers significant plastic deformation, whereas beyond δ, the material remains undeformed however not unaffected by temperature and microstructural changes.

The same way a viscous boundary layer surrounds a body moving through a fluid, the presence of a thin shear layer around the pin during a FSW process allows that a similar analysis can be performed. In a fluid, the boundary layer is defined as the region where the inertial and viscous forces balance each other. Similarly, the shear layer can be defined as the region where heat generation and heat transfer is balanced. Outside the boundary layer in a fluid, the region is controlled by inviscid flow, just as FSW where the outer region of the shear layer is predominantly heat conduction. The problem is solved for both regions, outside and inside the shear layer and both asymptotic solutions must be matched at their boundary, at the edge of the shear layer. This approach is known as "matched asymptotics".

2.3.1 Model simplifications

To simplify mathematical treatment, this problem will be restricted to systems that fulfill the conditions below:

1. The traveling pin can be considered a steady state, slow moving heat source. For this condition isotherms near the pin can be considered circular and heat transfer through the work-piece can be estimated using Rosenthal's solution. [45, 46] The slow moving heat source can be described as a function of the Peclet number given by:

$$Pe = \frac{Va}{2\alpha_\delta} \ll 1 \tag{2.1}$$

   where V is the tool travel speed, a is the pin radius and α_δ is the is the thermal diffusivity of the base plate material at a critical temperature T_δ, which will be defined later.

2. There is small advance per revolution of the tool. This condition allows the consideration of symmetry for the shear layer due to the fact that a small difference between the advancing and retreating side can be considered. If the incoming mass is smaller than the amount of mass moved in the shear layer, this condition can be described as:

$$Va \ll \omega a \delta \tag{2.2}$$

   where ω is the tool rotation speed and δ is the thickness of the shear layer as it was described before.

3. The shear layer is thin. This condition relates to the boundary layer explained before, meaning that the layer surrounding the pin is thin and does not have a geometry of its own. This condition can be expressed as:

$$\delta \ll a \tag{2.3}$$

4. The shoulder has a secondary influence on the maximum temperature near the pin. This condition states that peak temperature near the pin is affected mainly by heat produced from deformation instead of heat produced by the shoulder which tend to be more distributed in the work-piece. It is noteworthy that this assumption does not neglect heat generated by the shoulder. This condition can be expressed as:

$$T_p - T_\infty \ll \widehat{T_{max}} - T_\infty \tag{2.4}$$

where T_p is the preheat temperature due to the shoulder, T_∞ is the temperature of the plate far from the pin and the shoulder and $\widehat{T_{max}}$ is the temperature of the base material at the interface with the pin. All these temperatures will be defined later.

The first three conditions stated above allows the possibility to consider that heat transfer and plastic deformation around the tool can be approximated as a one dimensional problem, where the origin is located at the pin/work-piece interface perpendicular to it. The fourth condition opens up the consideration that the coupling between the thermal effect of the shoulder and that of the pin is weak.

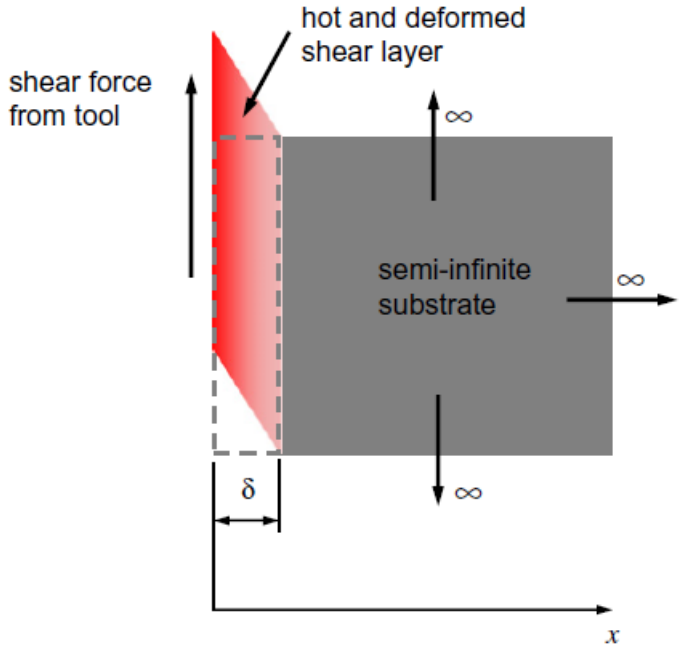

Figure 2.2: Schematic of the one-dimensional problem. x=0 is located in the pin/work-piece interface. [2]

2.3.2 Scaling of the coupled thermal and mechanical problem

In contrast with isothermal models of the shear layer that assume that the characteristic length scale for heat transfer is much larger than for plastic deformation, this coupled model consider that both phenomena occur within the same length scale: the thickness of the shear layer δ. On the other hand, similarly to how is done in [2], the problem can be divided in four sections, each one with its ordinary differential equations. Every section is solved using scaling analysis into four algebraic equations with four unknowns, with each unknown being a characteristic value of a function or differential expression. The analysis presented below uses the modified description of temperature profile in the shear layer to obtain estimates for:

- Maximum temperature in the shear layer.
- Thickness of the shear layer.
- Heat generated in the shear layer.
- Shear stress in the shear layer.

Heat transfer in the shear layer

In Figure 2.3, the temperature profile in the shear layer is presented when heat losses into the pin are considered. In the pin/work-piece interface ($x = 0$) the temperature is defined as T_S. Moving away from the pin into the shear layer, temperature increases until the maximum T_{max} is reached at ($x = x_{max}$). After that, temperature decreases monotonically from T_{max} to T_δ. This last value T_δ is used as the characteristic value that represents the transition between the shear layer and the undeformed material in the work-piece, at ($x = \delta$). Past δ, the model considers no plastic deformation and above it, significant plastic deformation is considered. Although in reality this transition is not sharp and occurs within a range, this is very narrow and can be reasonably neglected.

Peclet number for this analysis on FSW can be based on three different systems. The first one can be based on the circumferential length of the pin and its tangential velocity. This Peclet number is usually larger than 1. The second one is based on the tangential velocity and thickness of the shear layer. In this case, the Peclet number is usually smaller than 1. And finally, the Peclet number can be based on the pin radius and the travel velocity. This one is usually small and is the same one described in the first condition in Section 2.3.1. The Peclet number of the first two systems help to understand that heat transfer in the shear layer is primarily advective in the circumferential direction and conduction in the radial direction.

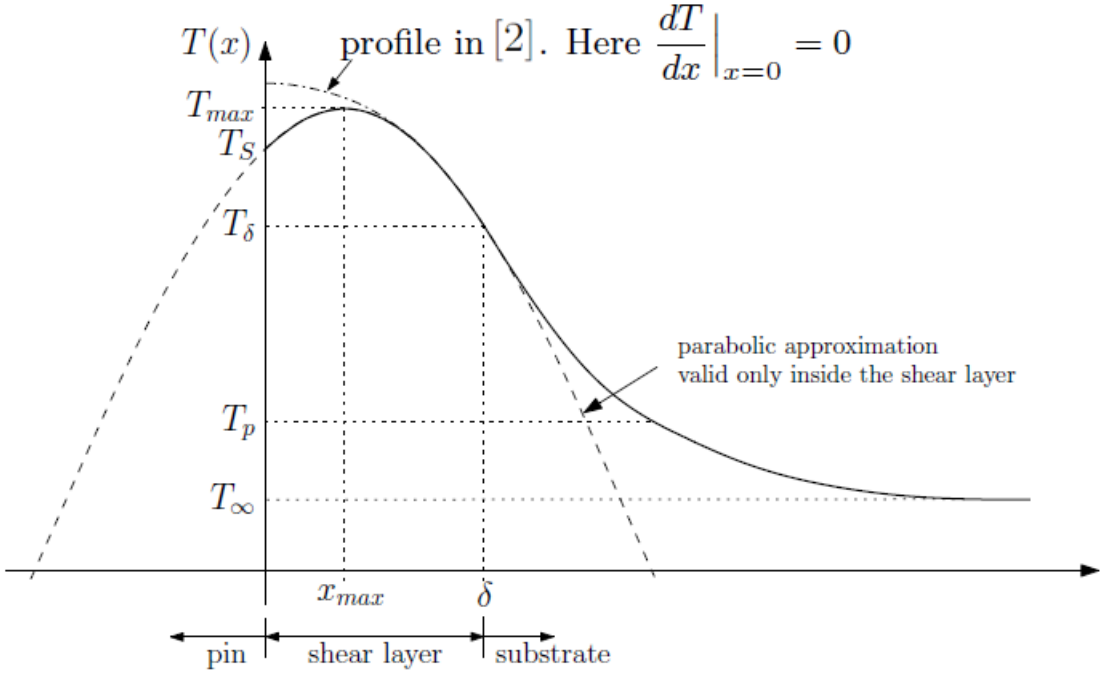

Figure 2.3: Temperature profile in the shear layer and surrounding material.

Following the analysis done in [2], the governing equation and boundary conditions for a pseudo-steady-state, low-Peclet, one-dimensional formulation of the problem are:

$$\frac{\mathrm{d}^2T}{\mathrm{d}x^2} + \frac{q''(x)}{k} = 0 \tag{2.5}$$

$$T|_{x=\delta} = T_\delta \tag{2.6}$$

$$\left[k(T)\frac{\mathrm{dT}}{\mathrm{d}x}\right]_{x=0} = q''_{out} \tag{2.7}$$

where $T(x)$ is the temperature in the shear layer, $q''(x)$ is the volumetric heat generation due to plastic deformation, $k(T)$ is the thermal conductivity of the base metal and q''_{out} is the heat flow that goes out from the shear layer into the pin. Revisiting Figure 2.3, the temperature profile in [2] shows the maximum temperature at the pin/work-piece interface because heat loss to the tool was not considered significant ($dT/dx|_{x=0} = 0$). Now as heat losses are considered, maximum temperature is lower and temperature at the pin/work-piece interface show a positive gradient ($dT/dx|_{x=0} > 0$).

Next, scaling analysis is applied to the dependent and independent variables in Equation 2.5 for further treatment by an estimation of their characteristic values. The normalized governing equation can be expressed as:

$$\left(\frac{\mathrm{d}^2\mathrm{T}}{\mathrm{d}x^2}\right)_c \left(\frac{\mathrm{d}^2\mathrm{T}}{\mathrm{d}x^2}\right)^* + \frac{q''_c}{k_\delta}\left(\frac{q''}{k}\right)^* = 0 \tag{2.8}$$

where $(d^2T/dx^2)_c$ and q''_c are estimates of characteristic values: maximum second derivative of temperature, and maximum volumetric heat generation respectively, k_δ in the thermal conductivity at T_δ and the quantities with an asterisk are dimensionless functions which extreme values are approximately -1 or 1.

Heat loss decreases the process efficiency and can happen mainly through four different paths; through the pin, through the shoulder, through the backing plate and through convection. The last two mentioned here will be explained later on, while the first two are included in this analysis to maximize temperature gradient near the pin, although it turns out to be small. The efficiency of the process (η) can be expressed in terms of the heat flow that is dissipated out of the shear layer into the pin (q''_{out}) (check Equation 2.7) and heat flow into the shear layer (q''_{in}) as:

$$\eta = \frac{q''_{in}}{q''_{in} + q''_{out}} \tag{2.9}$$

with q''_{in} as:

$$q''_{in} = \left[-k(T) \frac{\mathrm{dT}}{\mathrm{d}x} \right]_{x=\delta} \tag{2.10}$$

Process efficiency in Equation 2.9 is valid when the shear layer is thin. In this way, heat flow in the axial direction is small and the surface through which heat is transferred from the shear layer to the pin and into the shear layer is roughly the same size. As the thickness of the shear layer is $x = \delta$, it was mentioned before that temperature and thermal conductivity at this point are T_δ and k_δ respectively. Thus, the temperature profile in the shear layer can be scaled as follows.

The parabolic approximation showed in Figure 2.3 allows estimating the temperature using the standard quadratic equation given the vertex and a point. The vertex (h, k) is equal to (x_{max}, T_{max}) and the point (x, y) is (δ, T_δ). Then, the quadratic equation is given by:

$$(x - h)^2 = 4p(y - k) \tag{2.11}$$

Replacing the vertex and the point in 2.11, p is given by:

$$p = \frac{(\delta - x_{max})^2}{4(T_\delta - T_{max})} \tag{2.12}$$

Next, replacing 2.12 and the vertex in 2.11, temperature is given by:

$$T(x) = \frac{(x - x_{max})^2}{(\delta - x_{max})^2}(T_\delta - T_{max}) + T_{max} \tag{2.13}$$

where $x = \delta x^*$ and $x^*_{max} = x_{max}/\delta$. Then:

$$T(x) = T_\delta + (T_{max} - T_\delta)\left[1 - \left(\frac{x^* - x^*_{max}}{1 - x^*_{max}}\right)^2\right] \tag{2.14}$$

In equation 2.14, the term in brackets is replaced by Θ, leaving:

$$T(x) = T_\delta + (T_{max} - T_\delta)\Theta^*(x^*) \tag{2.15}$$

The maximum temperature T^*_{max} and its location x^*_{max} are values that need to be calculated. This dimensionless temperature has a maximum value of 1 at $x^* = x^*_{max}$ and a minimum value of zero at $x^* = 1$. This approximation is used to calculate $(dT/dx)_{x^*=0}$ for q''_{out} in Equation 2.7 and $(dT/dx)_{x^*=\delta}$ for q''_{in} in Equation 2.10. To calculate the general form of (dT/dx), the chain rule for finding derivatives is used:

$$\frac{\mathrm{dT}}{\mathrm{d}x} = \frac{\mathrm{dT}}{\mathrm{d}\Theta^*}\frac{\mathrm{d}\Theta^*}{\mathrm{d}x^*}\frac{\mathrm{d}x^*}{\mathrm{d}x} = (T_{max} - T_\delta)\frac{\mathrm{d}\Theta^*}{\mathrm{d}x^*}\frac{1}{\delta} \tag{2.16}$$

where

$$\frac{\mathrm{d}\Theta^*}{\mathrm{d}x^*} = \frac{-2(x^* - x^*_{max})}{(1 - x^*_{max})^2} \tag{2.17}$$

then, q''_{out} and q''_{in} are equal to:

$$q''_{out} = k_\delta \frac{T_{max} - T_\delta}{\delta}\frac{2x^*_{max}}{(1 - x^*_{max})^2} \tag{2.18}$$

$$q''_{in} = k_\delta \frac{T_{max} - T_\delta}{\delta}\frac{2}{(1 - x^*_{max})} \tag{2.19}$$

Finally, replacing Equation 2.18 and 2.19 in 2.9, the total efficiency of the process is obtained as:

$$\eta = 1 - x^*_{max} \tag{2.20}$$

This relevant expression establishes one of the unknowns in the temperature profile in the shear layer (x^*_{max}) as a function of the process efficiency, which is often known or measurable. To determine the other unknown parameter (T^*_{max}), the parabolic approximation is used to estimate $(d^2T/dx^2)_c$ in Equation 2.8. Then, using the chain rule:

$$\frac{\mathrm{d}^2\mathrm{T}}{\mathrm{d}x^2} = \frac{\mathrm{d}}{\mathrm{d}x^*}\left(\frac{\mathrm{dT}}{\mathrm{d}\Theta^*}\frac{\mathrm{d}\Theta^*}{\mathrm{d}x^*}\frac{\mathrm{d}x^*}{\mathrm{d}x}\right)\frac{\mathrm{d}x^*}{\mathrm{d}x}$$

$$= \frac{\mathrm{dT}}{\mathrm{d}\Theta^*} \frac{\mathrm{d}^2\Theta^*}{\mathrm{d}x^{*2}} \left(\frac{\mathrm{d}x^*}{\mathrm{d}x}\right)^2$$

$$= \frac{T_{max} - T_\delta}{\delta^2} \frac{-2}{(1 - x^*_{max})^2} \tag{2.21}$$

As the second derivative of a parabola is independent of the independent variable, the second derivative of the temperature does not depend of the location in the shear layer. Then, considering Equation 2.20, $(d^2T/dx^2)_c$ can be estimated as:

$$\left(\frac{\mathrm{d}^2\mathrm{T}}{\mathrm{d}x^2}\right)_c = 2\frac{T_{max} - T_\delta}{\delta^2\eta^2} \tag{2.22}$$

Because by definition characteristic values are positive, the negative sign was dropped. Then, the normalized equation of heat conduction in the shear layer is then expressed by:

$$\frac{2(T_{max} - T_\delta)}{\delta^2\eta^2} \left(\frac{\mathrm{d}^2\mathrm{T}}{\mathrm{d}x^2}\right)^* + \frac{q''_c}{k_\delta} \left(\frac{q''}{k}\right)^* = 0 \tag{2.23}$$

Then, Equation 2.23 yields the following algebraic equation:

$$-\frac{2(\widehat{\Delta T_{max}})}{\widehat{\delta}^2\eta^2} + \frac{\widehat{q''_c}}{k_\delta} = 0 \tag{2.24}$$

where $\Delta T_{max} = T_{max} - T_\delta$ and the values with hat "$\widehat{\ }$" represent estimations based on algebraic equations considering only dominant factors. Similarly to [2], estimation of the temperature at the pin/work-piece interface $\widehat{T_S}$, can be calculated evaluating Equation 2.14 at $x = 0$, getting:

$$\widehat{T_S} = \left(\frac{2\eta - 1}{\eta^2}\right) \widehat{\Delta T_{max}} + T_\delta \tag{2.25}$$

Heat generation in the shear layer

As the temperature profile changed in the shear layer for the revised formulation, the estimation for the heat generation must be revised. Following [2] analysis, the volumetric heat generation by plastic deformation is expressed by:

$$q''(x) = \eta_s \tau(x) \dot{\gamma}(x) \tag{2.26}$$

where η_s is the efficiency of the mechanical energy converted into heat without accounting for the small amount that is stored in the form of lattice defects, $\tau(x)$ is the shear stress experienced by an element of volume at coordinate x and $\dot{\gamma}(x)$ is the corresponding shear rate.

The normalized counterpart of Equation 2.26 is:

$$q_c'' q''^*(x^*) = \eta_s \tau_c \tau^*(x^*) \dot{\gamma}_c \dot{\gamma}^*(x^*) \tag{2.27}$$

where q_c'', τ_c and $\dot{\gamma}_c$ are unknown estimates considering a parabolic temperature variation within the shear layer. Then, the associated algebraic equation resulting from scaling is:

$$\widehat{q_c''} = \eta_s \widehat{\tau_c} \widehat{\dot{\gamma}_c} \tag{2.28}$$

For Equation 2.28 there is no direct way of estimating $\widehat{\dot{\gamma}_c}$, but the kinematic relationships from continuum mechanics indicate that the shear rate can also be expressed as $\dot{\gamma} = -(dv/dx)$, where $v(x)$ is the transverse velocity of the metal experiencing plastic shear. So, the next relationships can be stated:

$$\dot{\gamma}_c = -\left(\frac{\mathrm{d}v}{\mathrm{d}x}\right)_c \tag{2.29}$$

$$\dot{\gamma}^* = -\left(\frac{\mathrm{d}v}{\mathrm{d}x}\right)^* \tag{2.30}$$

The relationships stated above are useful because the rotational velocity of the pin can be used to calculate the characteristic value. Considering that the velocity of plastic deformation can be neglected ($v(\delta) \approx 0$) at $x = \delta$, solving the derivative:

$$v(\delta) - v(0) = \int_0^\delta \frac{\mathrm{d}v}{\mathrm{d}x} dx = 0 - \omega a \tag{2.31}$$

$$\omega a = -\widehat{\delta} \left(\frac{\mathrm{d}v}{\mathrm{d}x}\right)_c \int_0^1 \left(\frac{\mathrm{d}v}{\mathrm{d}x}\right)^* dx^* \tag{2.32}$$

$$\omega a = \widehat{\delta} \left(\frac{\mathrm{d}v}{\mathrm{d}x}\right)_c \int_0^1 \dot{\gamma}^* dx^* \tag{2.33}$$

Then, as it will be explained later, because of the high temperatures typical of FSW, the temperature and shear rate can be estimated with a linear behavior represented by:

$$\dot{\gamma}^* \approx \frac{T - T_\delta}{T_{max} - T_\delta} = \Theta^*(x^*) \tag{2.34}$$

simplifying the calculations. Then, replacing $\Theta^*(x^*)$ in Equation 2.15 and Equation 2.34 in 2.33, the characteristic value $(dv/dx)_c$ can be calculated as:

$$\widehat{\delta}\left(\frac{\mathrm{d}v}{\mathrm{d}x}\right)_c \int_0^1 \left[1 - \left(\frac{x^* - x^*_{max}}{1 - x^*_{max}}\right)^2\right] dx^* = \omega a \tag{2.35}$$

$$\widehat{\delta}\left(\frac{\mathrm{d}v}{\mathrm{d}x}\right)_c \left[1 - \frac{1}{\eta^2}\left(\frac{1}{12} + \left(\eta - \frac{1}{2}\right)^2\right)\right] = \omega a \tag{2.36}$$

$$\left(\frac{\mathrm{d}v}{\mathrm{d}x}\right)_c = \frac{\omega a}{\widehat{\delta}\zeta} \tag{2.37}$$

where ζ is a function of the total efficiency of the process represented in Figure 2.4. It must be emphasized that the efficiency η in Equation 2.36 considers only the pin. Some of the heat goes into the shoulder but for this work is not considered.

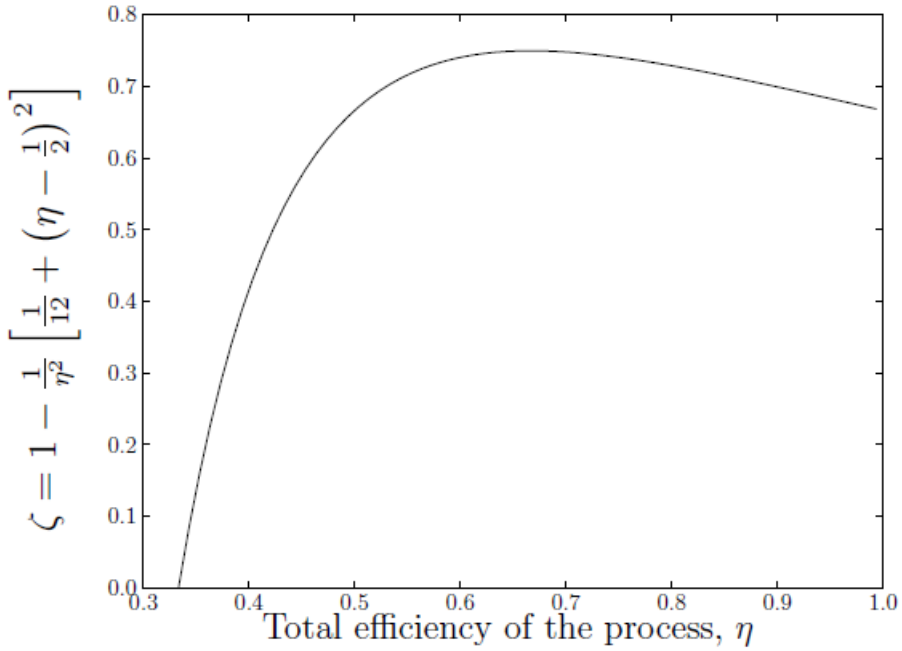

Figure 2.4: Function ζ to calculate the effect of heat losses on the temperature profile.

Finally, Equation 2.28 can be expressed by:

$$\widehat{q''_c} = \eta_s \widehat{\tau}_c \frac{\omega a}{\widehat{\delta}\zeta} \tag{2.38}$$

Now, two equations and four unknowns are involved in the analysis. As Mendez *et al.* [2] developed in his work, the remaining equations are obtained from the constitutive behavior in the shear layer and heat trasfer outside the shear layer.

Constitutive behavior in the shear layer

As there are currently no measurements done on materials that undergo the mechanical behavior expected during a FSW process such as deformation at high temperature and strain rates, the mechanical response of the material is modeled using Zener-Hollomon's constitutive model. This model relates effects of high temperature, stress and strain rate and is widely used in FSW models. [8, 38]

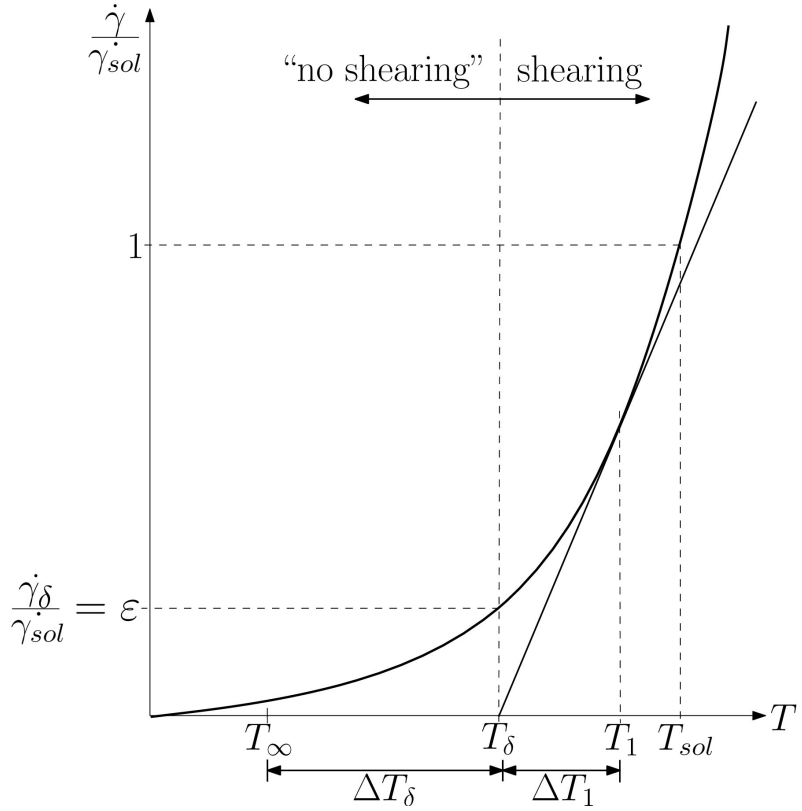

Figure 2.5: Constitutive behavior of the work-piece material. Strain rates below $\dot{\gamma}_\delta/\dot{\gamma}_{sol} = \varepsilon$ are considered negligible.

The expression of a Zener-Hollomon constitutive behavior is given by:

$$\dot{\gamma} = A\left(\frac{\tau}{\tau_R}\right)^n exp\left(-\frac{Q}{RT}\right) \tag{2.39}$$

where A, Q and n are the parameters of the constitutive model, R is the gas constant and τ_R is an arbitrary reference stress. For this work, the flow shear stress of reference is calculated by:

$$\tau_R = \frac{\sigma_R}{\sqrt{3}} \tag{2.40}$$

which is based on the distortion energy theory or the Von Mises criterion in uniaxial tension and pure shear.

Figure 2.5 illustrates schematically the behavior of the material in the work-piece. The vertical axis indicates the ratio between the shear rate and the shear rate at the solidus temperature (T_{sol}). The figure also shows the limit between the shear layer and the rest of the work-piece at T_δ, similarly to Figure 2.3. At this temperature, the ratio is defined as ε and below this value, plastic deformation is considered negligible. On the other hand, as it was proposed in [2], the best practical use of the constitutive model is when it is linearized. The proposed linearization following Figure 2.5 can be expressed by:

$$exp\left(-\frac{Q}{RT}\right) \approx \begin{cases} 0 & if \quad T \leq T_\delta \\ \frac{T-T_\delta}{T_1-T_\delta} exp(-\frac{Q}{RT_1}) & if \quad T > T_\delta \end{cases} \tag{2.41}$$

where T_1 is the temperature at which the linearization is tangent to the curve of the constitutive law. Also, this temperature is close to the solidus temperature of the work-piece material (T_{sol}). The relationship between T_1 and T_δ is:

$$T_1 - T_\delta = \frac{RT_1^2}{Q} \tag{2.42}$$

In the previous work [2], it was considered that $T_\delta = T_0 = T_{sol}(1 - RT_{sol}/Q)$, such that $T_1 = T_{sol}$. With T_0 as a threshold, temperature estimates resulted higher than measurements, suggesting that at T_0 the shear rate might not be negligible as assumed. Alternatively, T_δ is obtained using the constitutive model, so for a given choice of ε, the temperature T_δ is independent of the shear stress, as it is shown next:

$$T_\delta = T_{sol}\left(1 - \frac{RT_{sol}}{Q} ln(\varepsilon)\right)^{-1} \tag{2.43}$$

Finally, replacing the estimates in Equation 2.39 of the constitutive model, using the characteristic values, the following equation is obtained:

$$\frac{\omega a}{\widehat{\delta}\zeta} \approx AB'\left(\frac{\widehat{\tau}_c}{\tau_R}\right)^n \frac{\widehat{\Delta T_{max}}}{\Delta T_1} \tag{2.44}$$

where $\Delta T_1 = T_1 - T_\delta$ and $B' = exp(-Q/RT_1)$. The values of T_δ and T_1 depend only on the materials properties (which are known) and on the choice of threshold shear rate ε. The value of ε is unknown and in this work will be determined empirically by best match to available data. It is important to note that no unknowns are introduced in Equation 2.44.

Heat conduction outside the shear layer

Outside the shear layer, heat is transmitted by conduction through the work-piece. As it was mentioned before, for a slow moving heat source, Rosenthal's thin plate solution [45] can be considered. The scaled equation of heat conduction outside the shear layer is given by:

$$\Delta T_\delta = T_\delta - T_\infty = \eta\eta_s \frac{\omega a^2 \widehat{\tau_c}}{k_\delta} K_0(\xi) \tag{2.45}$$

with

$$\xi = \sqrt{\left(\frac{V}{2\alpha_\delta}\right)^2 + \frac{h+h'}{k_\delta d} r} \tag{2.46}$$

where α_δ is the thermal diffusivity of the work-piece material at T_δ, h and h' are the coefficients for convection heat losses on the top of the plate (typically 10 W/m^2K) and heat losses to the anvil on the bottom (typically 10.000 W/m^2K for contact resistance), d is the plate thickness and r correspond to a radial distance from the line heat source. The symbol K_0 corresponds to the modified Bessel function of a second kind and order 0. Finally, Equation 2.46 does not add any new unknown characteristic value.

2.3.3 Scaling expressions for the coupled thermomechanical system

Equations 2.24, 2.38, 2.44 and 2.45 constitute a system of four equations and four unknowns. The solution of said set of equations is:

$$\widehat{\delta} = a \left[2\frac{\Delta T_1}{AB'} \left(\frac{a^2 \tau_R \eta_s}{k_\delta}\right)^n \left(\frac{K_0 \omega}{\Delta T_\delta}\right)^{n+1} \eta^{n-1} \right]^{\frac{1}{2}} \tag{2.47}$$

$$\widehat{\Delta T_{max}} = \Delta T_1 \left[\frac{1}{2AB'\Delta T_1 \zeta^2} \left(\frac{K_0 \omega}{\Delta T_\delta}\right)^{n-1} \left(\frac{a^2 \tau_R \eta_s}{k_\delta}\right)^n (\omega\eta)^{n+1} \right]^{\frac{1}{2}} \tag{2.48}$$

$$\widehat{q_c''} = \left[\frac{AB'}{2\Delta T_1 \zeta^2} \left(\frac{1}{\tau_R \eta_s}\right)^n \left(\frac{1}{\omega\eta}\right)^{n+1} \left(\frac{k_\delta}{a^2}\right)^{n+2} \left(\frac{\Delta T_\delta}{K_0}\right)^{n+3} \right]^{\frac{1}{2}} \tag{2.49}$$

$$\widehat{\tau_c} = \frac{k_\delta \Delta T_\delta}{\eta\eta_s \omega a^2 K_0} \tag{2.50}$$

Together with these equations, torque can be estimated using Equation 2.50 by:

$$\widehat{M_p} = 2\pi \widehat{\tau_c} a^2 d \tag{2.51}$$

where a is the radius of the pin and t is the thickness of the plate.

These equations are closed-form expressions with unique characteristics and have the form of power laws. Some of the characteristics are:

- They are independent of the work-piece material.
- The estimations are based on parameters independent of the process. Therefore, is not necessary to measure torque or temperature to make predictions. By knowing the material and process parameters, an estimation can be carried out.
- During FSW process design, these values can be extremely useful. Thermophysical values can be obtained from said parameters and, due to power laws being easily inverted, parameters can be estimated from desired thermophysical values.

Chapter 3

Methodology

3.1 Data Collection

To test the validity of the equations presented in Chapter 2, these estimations will be compared with results of simulations, numerical and experimental tests reported in the literature. Every relevant value reported in each test will be considered to generate an estimation under the same operation parameters. For maximum temperature data, in case of experimental tests, this measure is done using a thermocouple embedded in the work-piece and at times in the pin, while in simulations or numerical tests, peak temperature is calculated or presented in a software. Torque data was obtained from reported measurements of time average torque in steady state welds. Intrinsic errors of the collected data are not addressed in this work.

Other values that are relevant to this work and specific for every experiment are the tool travel speed, the tool rotation speed and the tool dimensions. As the tool pin comes in different shapes and forms [4], it is important to define the pin measurements. For a common straight cylindrical pin, the diameter of the base is considered. For a threaded pin, the threaded diameter of the bolt is considered. And for a linearly tapered pin, the diameter at the mid-point of the pin length is considered. Other types of pin such as Trivex^{TM}, MX triflute^{TM}, Flared triflute^{TM} are not considered in this work.

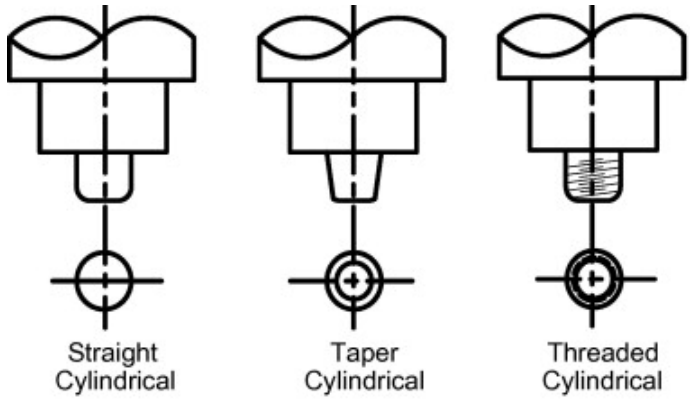

Figure 3.1: Types of pin shapes considered in this work.

Following the publications of Mendez *et al.* [2], this work considers the same database plus 96 new values compiled from 29 publications. Hence, a total of 280 values are considered to evaluate the estimations proposed. Furthermore, 10 new materials are added to the database, therefore the materials considered in the database are: seventeen aluminum alloys (AA1080, AA2024, AA2195, AA2198, AA2199, AA2219, AA2524, AA5059, AA5083, AA6061, AA6082, AA7010, AA7020, AA7050, AA7075, AA7136 and SSA038), five steels (IF, SAE1012, SAE1018, SAE1035 and 304SS), one titanium alloy (Ti-6Al-4V) and one magnesium alloy (AZ31).

3.2 Material Properties

As this work uses an updated version of the database used in [2], the properties for several materials can be obtained from that publication. In particular, the thermal and mechanical properties of AA2024, AA2195, AA5083, AA6061, AA7050, AA7075, SAE1018, 304SS and Ti-6Al-4V where reported in [2]. On the other hand, for those materials added to the data base, mechanical a thermal properties where obtained from different sources. Mechanical properties are often reported in the publication which the data comes from or in the Metals Handbook. [51,52] For thermal properties, some where found in the literature [53,54] and for the remaining materials a specific software was used.

3.2.1 JMatPro®

Because the thermophysical properties of materials change with temperature, values reported on the literature are often not useful in the case of FSW research since they represent the behavior of the material at room temperature (20-25°C). Therefore, properties such as the thermal conductivity and specific heat must be obtained by calculations or via software. JMatPro® is a simulation software that calculates several material properties and is particularly useful for multi-component alloys. The software requires the weight percent (as shown in Table A.1 and A.2) of the material and the temperature at which the properties want to be calculated. For this work, the solidus temperature was used to calculate the thermophysical properties of the materials.

3.2.2 Zener-Hollomon Constants

In the same way as material properties from [2] where used in this work, Zener-Hollomon law constants for those same materials (AA2024, AA2195, AA5083, AA6061, AA7050, AA7075, SAE1018, 304SS and Ti-6Al-4V) are taken from [2] and used here. As for the remaining materials, some of the constants where found in the literature [55–59] and others where copied from other materials of the same family and characteristics. In this sense, AA6082 used the constants from AA6061, AA7136 used the constants from SSA038, AA2199 used the constants from AA2198 and AA7020 used the constants from AA7010.

Table 3.1: Mechanical a thermal properties of the materials.

Material	$T_{solidus}$ (K)	k (W/ms)	c_p (J/kg)	ρ (kg/m^3)	σ_R (MPa)	η_s %
AA1080	913	211	1055	2680	100	100
AA2024	779	185	1100	2670	103	100
AA2195	747	196	1338	2770	692	100
AA2198	823	177	1170	2750	560	100
AA2199	823	151	1062	2780	560	100
AA2219	813	175	1020	2950	200	100
AA2524	820	177	1051	2820	200	100
AA5059	811	147	1261	2553	35	100
AA5083	812	147	1190	2523	214	100
AA6061	823	200	1160	2590	55	100
AA6082	853	179	1087	2710	60	100
AA7010	753	135	1170	2950	103	100
AA7020	883	148	1250	2900	103	100
AA7050	732	180	861	2827	455	100
AA7075	771	192	1109	2693	103	100
AA7136	783	115	1010	3150	380	100
SSA038	801	122	1114	3000	120	100
IF	1550	36	1290	7400	180	100
SAE1012	1600	34	900	7330	190	100
SAE1018	1665	33	699	7314	205	100
SAE1035	1700	31	700	7250	210	100
304SS	1666	33	720	7350	290	100
Ti-6Al-4V	1710	27	750	4198	875	100
AZ31	773	144	1446	1696	170	100

Unfortunately, the constants found in the literature does not capture the conditions under which FSW operates. For this, Sellars and Tegart [60] proposed an empirical constitutive equation applicable at low and high levels of stress. As explained by these authors, the deformation mechanisms operating in hot-working process at low stress can be described by:

$$\dot{\varepsilon} = A\left(\frac{\sigma}{\sigma_R}\right)^n exp\left(-\frac{Q}{RT}\right) \tag{3.1}$$

where A, Q and n are constants. This equation does not capture the behavior of the materials at high stress. So, the authors proposed the following equation:

$$\dot{\varepsilon}' = A'\left[sinh\left(\frac{\sigma'}{\sigma'_R}\right)\right]^{n'} exp\left(-\frac{Q'}{RT}\right) \tag{3.2}$$

where A', Q', n' and σ'_R are constants. Then, to use Equation 3.2 for a high stress-strain-temperature process like FSW, a relationship between the constants of Equations 3.1 and 3.2 must be found.

To incorporate the effect of Equation 3.2 into Equation 3.1, the procedure below must be followed:

1. Linearize both equations

$$\ln(\dot{\varepsilon}) = \ln A + n\ln\left(\frac{\sigma}{\sigma_R}\right) - \frac{Q}{RT} \tag{3.3}$$

$$\ln(\dot{\varepsilon'}) = \ln A' + n'\ln\left[sinh\left(\frac{\sigma'}{\sigma'_R}\right)\right] - \frac{Q'}{RT} \tag{3.4}$$

2. Calculate the partial derivatives of $\ln(\dot{\varepsilon})$ with respect to $1/T$ and $\ln(\sigma)$ for each equation in 1.

$$\frac{\partial \ln(\dot{\varepsilon})}{\partial 1/T} = -\frac{Q}{RT} \tag{3.5}$$

$$\frac{\partial \ln(\dot{\varepsilon})}{\partial \ln(\sigma)} = n \tag{3.6}$$

$$\frac{\partial \ln(\dot{\varepsilon'})}{\partial 1/T} = -\frac{Q'}{RT} \tag{3.7}$$

$$\frac{\partial \ln(\dot{\varepsilon})}{\partial \ln(\sigma)} = \frac{n'\sigma'}{\sigma'_R}\frac{1}{\tanh\left(\frac{\sigma'}{\sigma'_R}\right)} \tag{3.8}$$

3. Evaluate each equations presented in 2. at the solidus temperature of the alloy and at $\dot{\varepsilon} = 300(1/s)$, which is an average value of strain rate achieved during Friction Stir Welding.

$$\frac{Q}{RT} = \frac{Q'}{RT} \rightarrow Q = Q' \tag{3.9}$$

$$n = \frac{n'\sigma'}{\sigma'_R}\frac{1}{\tanh\left(\frac{\sigma'_R}{\sigma}\right)} \tag{3.10}$$

   Therefore, the values of constants Q and n can be calculated using Equations 3.9 and 3.10 respectively.

4. Now that Q, n, $\dot{\varepsilon}$ and T is known, those values can be replaced in Equation 3.3 to get A:

$$\ln(A) = \ln(\dot{\varepsilon}) - n\ln\left(\frac{\sigma'}{\sigma_R}\right) + \frac{Q}{RT_{solidus}} \tag{3.11}$$

Table B.1 shows the values of the Zener-Hollomon law constants for every material. Is important to note that some of the values of A', n' and Q' are repeated between materials but for A and n every value is different. This is the case of the materials which constants could not be found in the literature and were copied from similar materials. However, after applying the procedure shown above, constants change resulting in different constants for each material. In addition, AA5059 and AZ31 does not present values A', n' and σ'_R, this is because the constants for these materials are from FSW studies and the Zener-Hollomon constants are taken directly from these sources. [61, 62]

Chapter 4

Results

4.1 Ratio of measurement to estimation

To show how the estimations compare to measurements and numerical results, the ratio between both these values ($X/\widehat{X}$) is used. For this particular work, two ratios are used: maximum temperature ratio (Equation 4.1) and torque ratio (Equation 4.2). The terms with a hat represent the estimation calculated by the model and the term without the hat represent the term to a measurement/numerical result.

$$\Theta = \frac{T_{max} - T_\infty}{\widehat{T_{max}} - T_\infty} \tag{4.1}$$

$$M/\widehat{M} \tag{4.2}$$

Each ratio will be plotted against the following expressions:

$$Pe \tag{4.3}$$

$$\frac{V}{\omega\widehat{\delta}} \tag{4.4}$$

$$\frac{\widehat{\delta}}{a} \tag{4.5}$$

$$\frac{T_p - T_\infty}{T_{max} - T_\infty} \tag{4.6}$$

where each one represent the simplifications stated in Chapter 2, Equations 2.1, 2.2, 2.3 and 2.4 respectively. Two scenarios can occur for the given plots, for the case in which the simplifications become negligible, the ratio should tend to a constant value. This value should not be far from one, so that the estimations capture the same order of magnitude of the target variable. Conversely, if the ratio deviates from a constant value, the simplification affect the results, meaning that the simplification becomes relevant. In the later case, a correction function is applied so estimations are improved.

The improved estimations take forces neglected in the formulation of the scaling law into consideration. As a result, the estimations become closer to the measurement and numerical results. It is important to mention that numerical or experimental errors are inevitable in the data collected. Because of this, scatter in the ratio $(X/\widehat{X})$ is always going to be present.

The improvement of the estimations is developed using the following correction function:

$$f\left(Pe, \frac{\widehat{\delta}}{a}, \frac{V}{\omega\widehat{\delta}}, \frac{T_p - T_\infty}{\widehat{T_{max}} - T_\infty}\right) \tag{4.7}$$

$$= C_1(1 + C_2 Pe)^{C_3}\left(1 + C_4\frac{\widehat{\delta}}{a}\right)^{C_5}\left(1 + C_6\frac{V}{\omega\widehat{\delta}}\right)^{C_7}\left(1 + C_8\frac{T_p - T_\infty}{\widehat{T_{max}} - T_\infty}\right)^{C_9}$$

where $C_i (i = 1, 2, ..., 9)$ are constants fitted using a minimum least squares regression given by:

$$\phi = Min\sum_{i}^{n}\left(log\left(\frac{X}{\widehat{X}}\right)_i - log(f_i)\right)^2 \tag{4.8}$$

where n is the total number of data considered. If all the simplifications are neglected, C_1 accounts for mathematical errors induced by the scaling model. However, if the simplifications become relevant, coefficients beside C_1 capture a power law behavior. Then, the improved estimations are defined by:

$$\widehat{X}^+ = \widehat{X} \cdot f\left(Pe, \frac{\widehat{\delta}}{a}, \frac{V}{\omega\widehat{\delta}}, \frac{T_p - T_\infty}{\widehat{T_{max}} - T_\infty}\right) \tag{4.9}$$

It is important to mention that each simplification to the physics of the model has different contribution to the total error of the scaling model. Therefore, in some cases, just by applying one or some of the constants in Equation 4.7, improvements can be achieved. This is done to avoid an overuse of computational resources for marginally better results. Also, only experimental data is considered in this fitting. This allows for improvements based on real data and compare the behavior of simulations and numerical models to real experiments.

Two types of graphs will be analyzed. The first graphs will show the relation $(X/\widehat{X})$ versus each one of the simplifications in Chapter 2. In each of these graphs, only a subset of the data available is used. The subset in each graph consists of the data that fulfills all the simplifications except the one that is being used. So, for example, for the Θ *vs* Pe graph, $\widehat{\delta}/a, V/\omega\widehat{\delta}$ and $(T_p - T_\infty)/(T_{max} - T_\infty)$ must be less than 1.

The second type of graph relates the improved estimations $(\widehat{X}^+)$ with the numerical or experimental results (X). For these graphs, all the data available is considered. Table C.1 summarizes the data available. Additionally, for every graph presented in this section, simulations and numerical models can be easily differentiated from experimental points by noticing the color of the marker in the graph. Simulations and numerical models are represented by black markers where experimental points are represented by colored markers.

4.1.1 Optimization for estimations

Before composing the graphs for the estimations of maximum temperature and torque, the following optimization must be carried out:

$$\Pi = Min \sum_{i}^{n} \left[log\, T_{max} - log\left(C_1\, \Delta\widehat{T_{max}} + C_2\, T_\delta \right) \right]^2 \tag{4.10}$$

where n is the total number of data considered, T_{max} is the value of maximum temperature of the experiment and T_δ and $\Delta\widehat{T_{max}}$ are the values calculated from Equations 2.43 and 2.48. C_1 and C_2 are variables that can be adjusted for this optimization but due to the fact that they are very close to 1, for this work they are fixed at that value. Then, the only variable that minimizes Equation 4.10 is ε. As this value is relevant in the model, two scenarios are proposed. In the first case, ε is optimized using Equation 4.10 considering all the experimental data collected. On the other case, ε is optimized using the same procedure but the optimization is carried out for each family of materials. The materials are grouped in six families: AA2XXX, AA5XXX, AA6XXX, AA7XXX, Steel and Titanium as Table 4.1 shows. For the remaining family materials (AA1XXX, Magnesium and Stainless Steel) the optimized value of ε considering all materials is used. This is because there are very few points to carry out an optimization in each of these group of materials.

Table 4.1: Optimized value of ε found for the considered material families.

Material Family	Optimized ε
AA2XXX	8.11×10^{-5}
AA5XXX	2.16×10^{-3}
AA6XXX	1.66×10^{-4}
AA7XXX	3.13×10^{-5}
Steel	1.00×10^{-7}
Titanium	8.81×10^{-3}
All Materials	1.50×10^{-4}

4.2 Estimation of maximum temperature

4.2.1 Ratio of maximum temperature, optimizing for every material family.

For these graphs, the values of ε used are the ones optimized from all the experimental points of the data set, separated into groups depending on the family of the material (Table 4.1). Figures 4.1, 4.2, 4.3 and 4.4 present the ratio of maximum temperature as a function of the expressions in Equations 4.3 through 4.6 as it was mentioned before. The simplifications are not always satisfied for any of the graphs presented, nonetheless a fair amount of points do satisfy the conditions allowing interesting conclusions to be made.

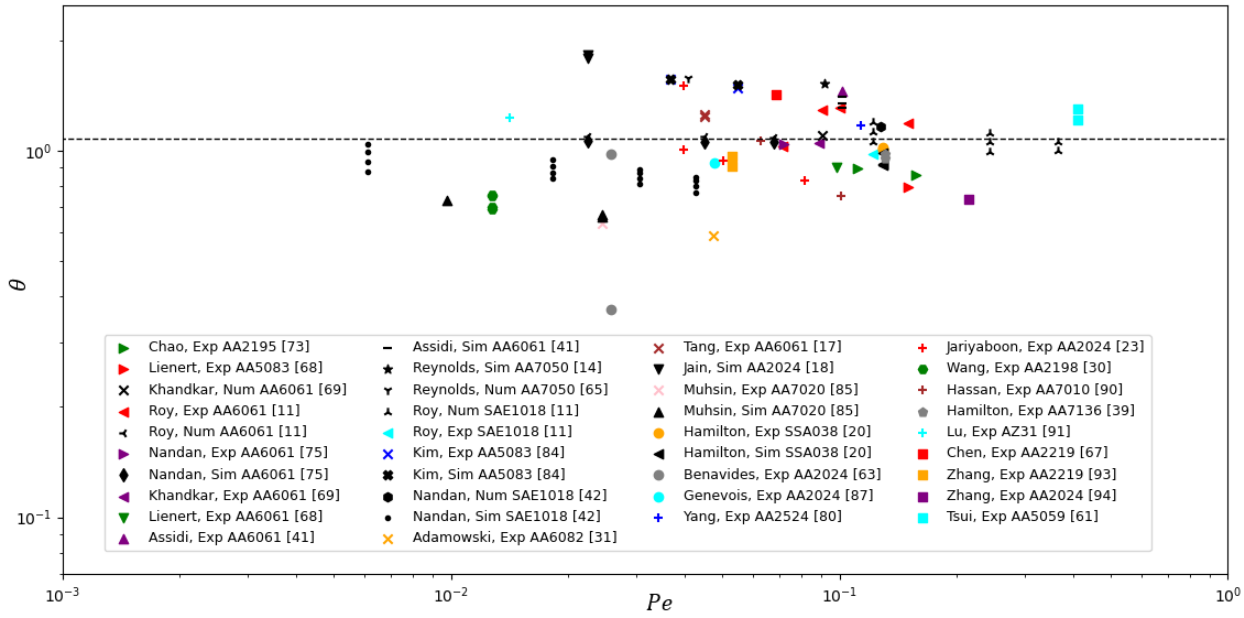

Figure 4.1: Ratio of maximum temperature as a function of Peclet Number. Different ε according to material family.

Figure 4.1 and 4.4 present the ratio of maximum temperature against the Peclet number (Pe) and $(T_p - T_\infty)/(\widehat{T_{max}} - T_\infty)$. It can be observed that all the points are distributed above and under the trendline given in Equation 4.11, between 0.7 and 2 with the exception of a couple of points from Benavides *et al.* [63] and Jain *et al.* [18] among others. It is fair to mention that experimental points are scattered in a wider range than numerical/simulation points across the horizontal axis for Figure 4.4. Additionally, temperature shows no clear dependence of Pe or $(T_p - T_\infty)/(\widehat{T_{max}} - T_\infty)$ as the points fall around a constant value of the temperature ratio.

Figure 4.2 presents the ratio of maximum temperature as a function of $(V/\omega\widehat{\delta})$. No clear dependence can be observed as all the points fall near the constant value of the trendline. In this case, an exceptionally wide range of values for the simplification $(V/\omega\widehat{\delta})$ of around 12 orders of magnitude can be observed, although the vast majority is concentrated between 10^{-3} and 10^{2} with a couple of exceptions from Wang *et al.* [30], Reynolds *et al.* [14], Fu *et al.* [21] among others. Once again, Benavides *et al.* [63] falls off the trendline.

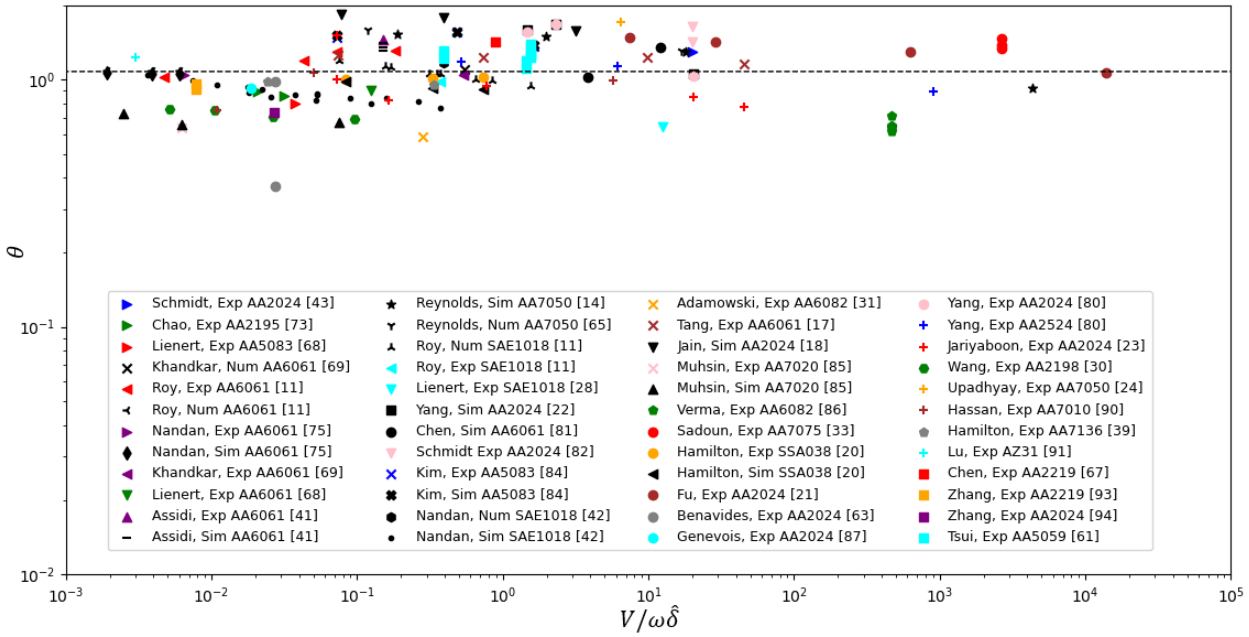

Figure 4.2: Ratio of maximum temperature as a function of $(V/\omega\widehat{\delta})$. Different ε according to material family.

Figure 4.3 shows the ratio of maximum temperature as a function of $(\widehat{\delta}/a)$. This graph differs from the others as a clear dependence of the maximum temperature is observed from the simplification $(\widehat{\delta}/a)$. For a value of $\widehat{\delta}/a > 1$, the ratio of temperature falls, reaching values close to 0.01. Regarding the points scattered in the graph, Benavides *et al.* [63] escapes from the trendline, as Lee *et al.* [64] and Adamowski *et al.* [31] does. Furthermore, most of the points observed past the unitary boundary are experimental with a couple of exceptions from Reynolds *et al.* [65].

The model underpredicts the estimation of maximum temperature by approximately 7% with an associated error of 9.835, as Figures 4.1, 4.2, 4.3 and 4.4 have shown. For the correction function, the conclusion reached in Karem Tello's thesis [66] is used. The case where C_1, C_4 and C_5 from Equation 4.7 are considered is selected for this work, as this fit requires less computing cost with adequate results.

Therefore, the correction function for the estimation of maximum temperature is given by:

$$f(\widehat{\delta}/a) = 1.077\left(1 + 0.3319\frac{\widehat{\delta}}{a}\right)^{-1.0099} \tag{4.11}$$

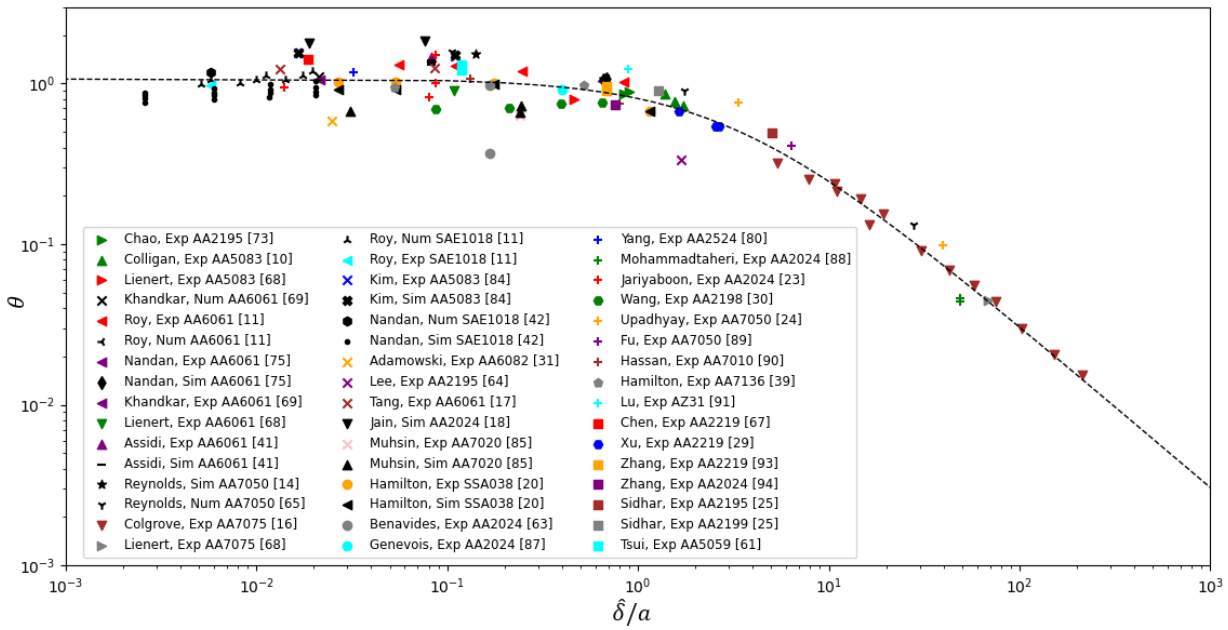

Figure 4.3: Ratio of maximum temperature as a function of $(\widehat{\delta}/a)$. Different ε according to material family.

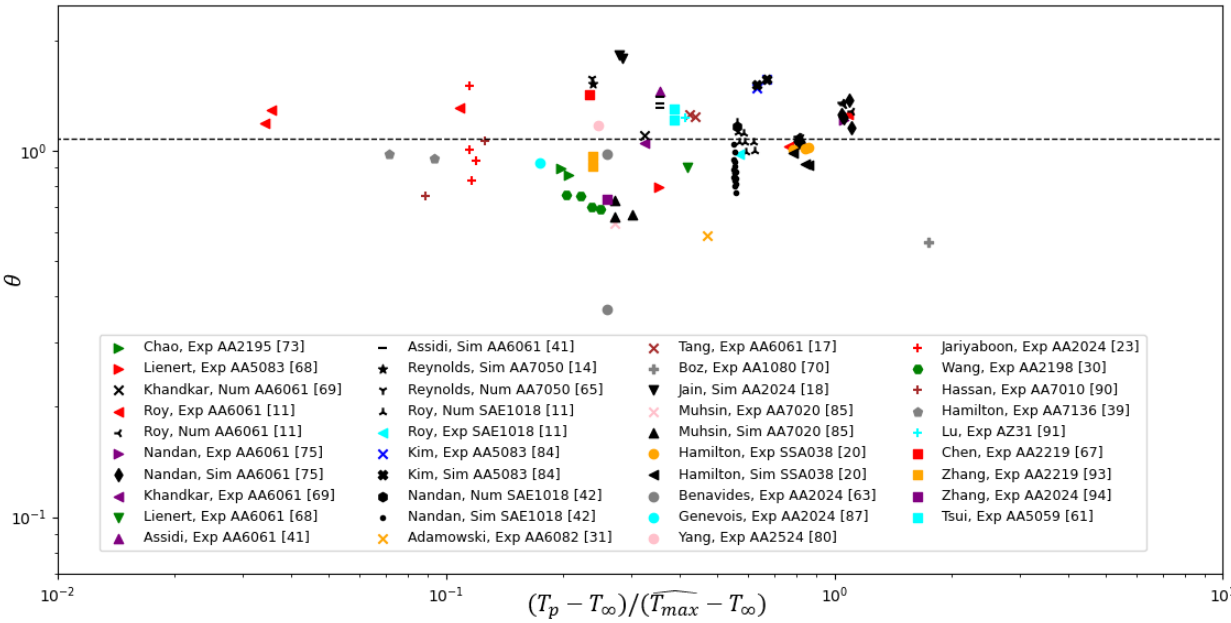

Figure 4.4: Ratio of maximum temperature as a function of $(T_p - T_\infty)/(\widehat{T_{max}} - T_\infty)$. Different ε according to material family.

The trendlines presented in Figures 4.1, 4.2 and 4.4 correspond to the correction function evaluated at $\widehat{\delta}/a = 0$. Finally, Figure 4.5 presents the correlation between measurement $(T_{max} - T_\infty)$ and improved estimation of the maximum temperature $(\widehat{T_{max}} - T_\infty)^+$ given by:

$$(\widehat{T_{max}} - T_\infty)^+ = (T_{max} - T_\infty) \cdot f(\widehat{\delta}/a) \tag{4.12}$$

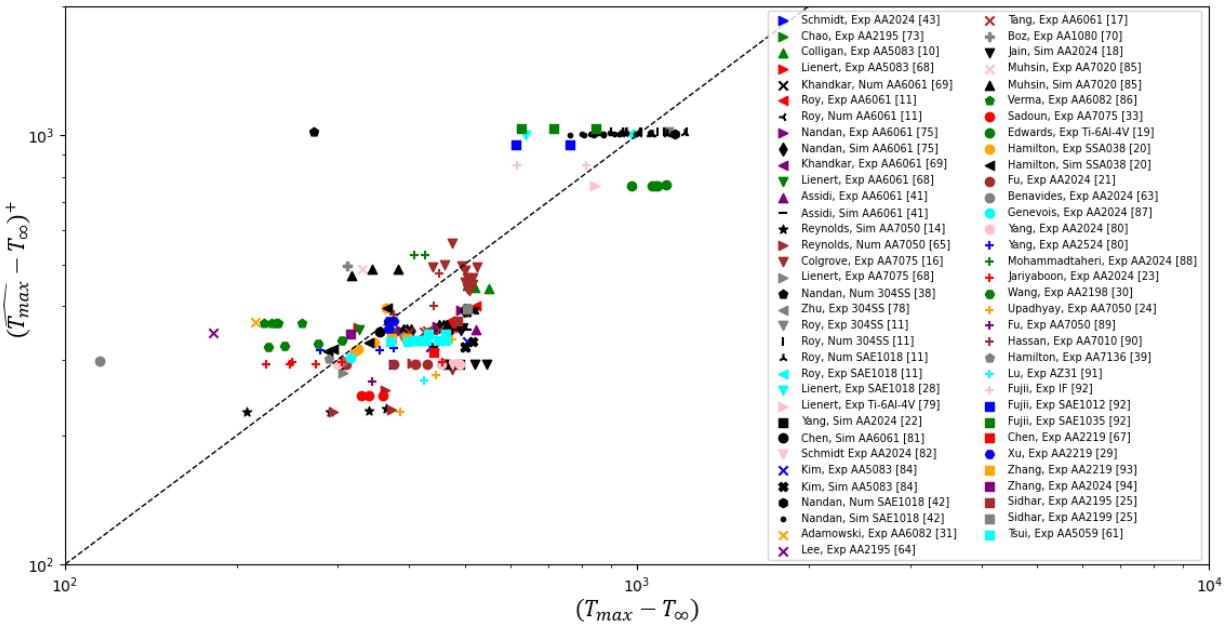

Figure 4.5: Correlation between the maximum temperature reported in the literature and the improved maximum temperature. Different ε according to material family.

Figure 4.5 presents all points with maximum temperature measurements versus the improved estimations. As it was expected, the majority of the points fall around the 1:1 trendline in the graph with a couple of exceptions. Once again, one point from Benavides *et al.* [63] fails to get close to the trendline together with a point from Nandan *et al.* [38], a numerical model on Stainless Steel. Types of material separate from each other as expected between steels and aluminum because of the typical temperatures reached during the process.

4.2.2 Ratio of maximum temperature, optimizing for all materials.

For these graphs, the value of ε is optimized from every material in the data set. This value can be found in Table 4.1 as 'All materials'. Same as before, Figures 4.6, 4.7, 4.8 and 4.9 present the ratio of maximum temperature as a function of the expressions in Equations 4.3 through 4.6. Few differences can be observed between the graphs when a single ε is optimized for all materials and the optimization for every group of materials.

Figure 4.9 present the ratio of maximum temperature against $(T_p - T_\infty)/(\widehat{T_{max}} - T_\infty)$. The graph shows how the points fall around the trendline given by Equation 4.13, although in this case the points are somewhat closer to the trendline than the same graph in the previous section (Figure 4.4). This is confirmed as the associated error equals 9.671. The points further from the line are the same as in Figure 4.4 and additional points that satisfy the conditions are present (Edwards *et al.* [19] and Tsui [61]). Figure 4.6, that present the ratio of maximum temperature against the Peclet number (Pe), show a very similar behavior to the graph in Figure 4.1 with additional points of Tsui [61] and the absence of Chen *et al.* [67].

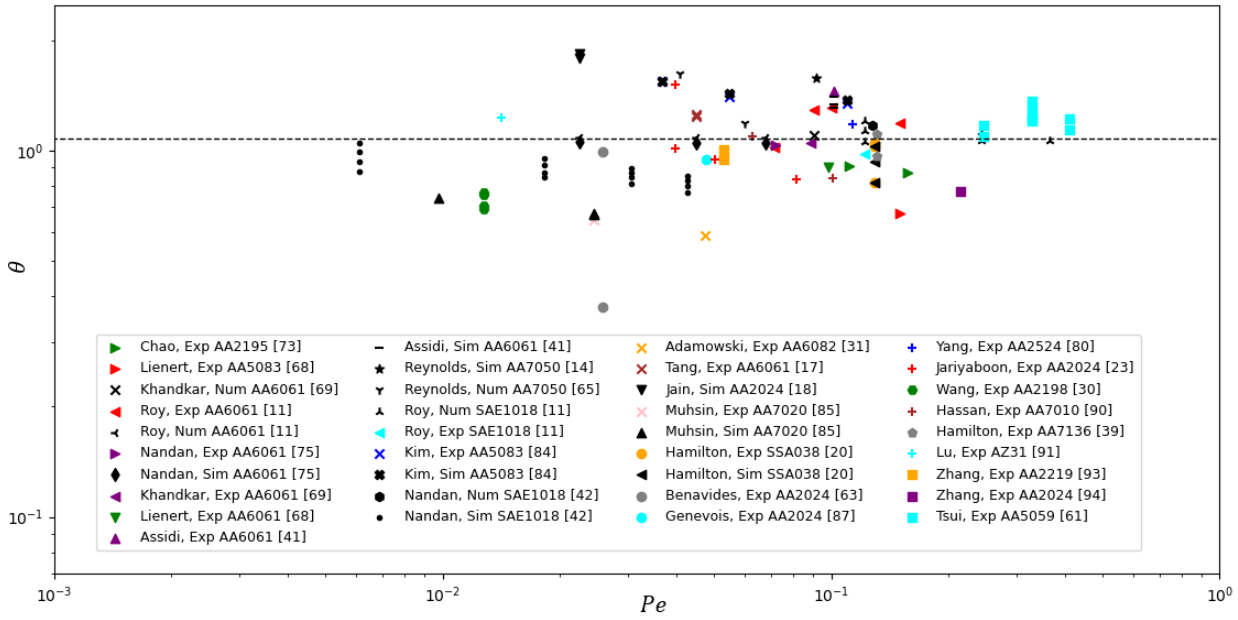

Figure 4.6: Ratio of maximum temperature as a function of Peclet Number. One ε for all materials.

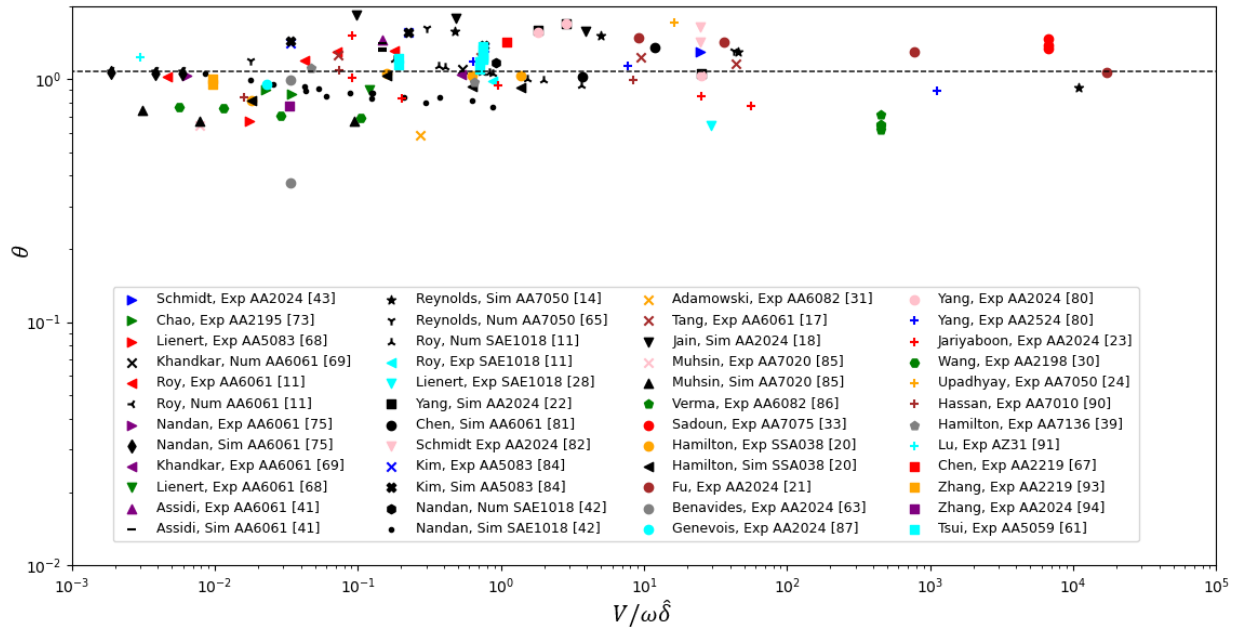

Figure 4.7: Ratio of maximum temperature as a function of $(V/\omega\widehat{\delta})$. One ε for all materials.

Figure 4.7 presents the ratio of maximum temperature as a function of $(V/\omega\widehat{\delta})$. No clear differences can be observed when compared to the graph in Figure 4.2 besides small shifts in some points. The range on the horizontal axis continues to be of about 12 orders of magnitude. A similar case is observed for Figure 4.8, where the trendline has the same behavior as in Figure 4.3. A clear dependence of $(\widehat{\delta}/a)$ is observed for the maximum temperature as a drop of the maximum temperature ratio occurs from $\widehat{\delta}/a > 1$ onwards. It is also worth noticing that a small shift can be observed when comparing Figure 4.8 with 4.3, where some points moved to higher values in the horizontal axis.

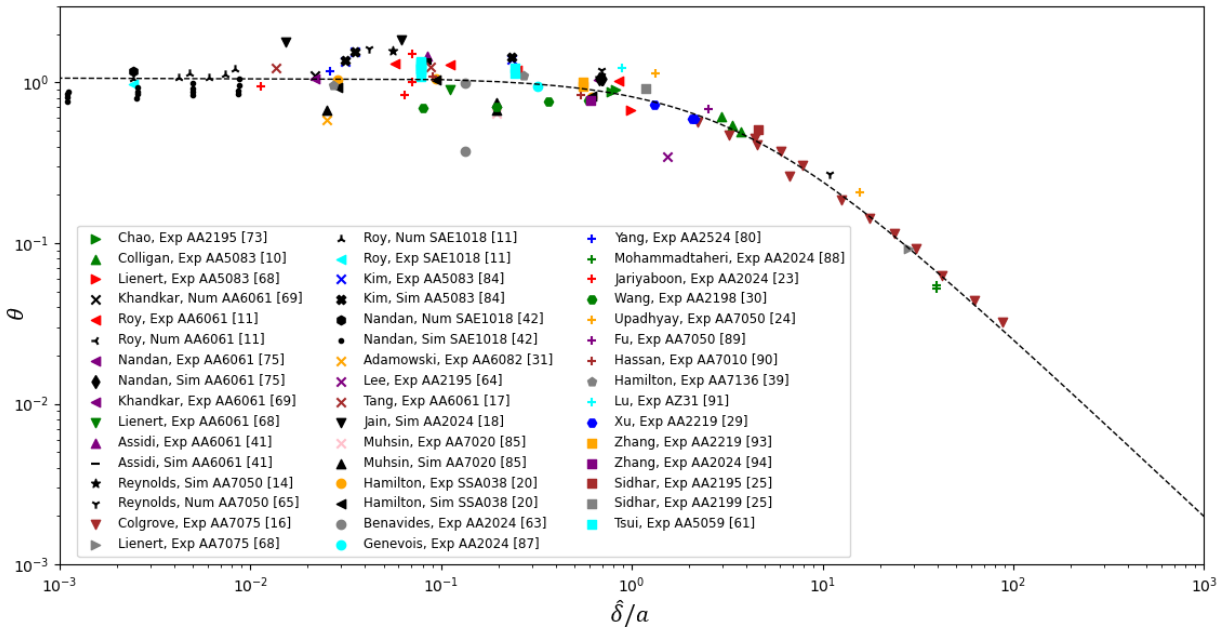

Figure 4.8: Ratio of maximum temperature as a function of $(\widehat{\delta}/a)$. One ε for all materials.

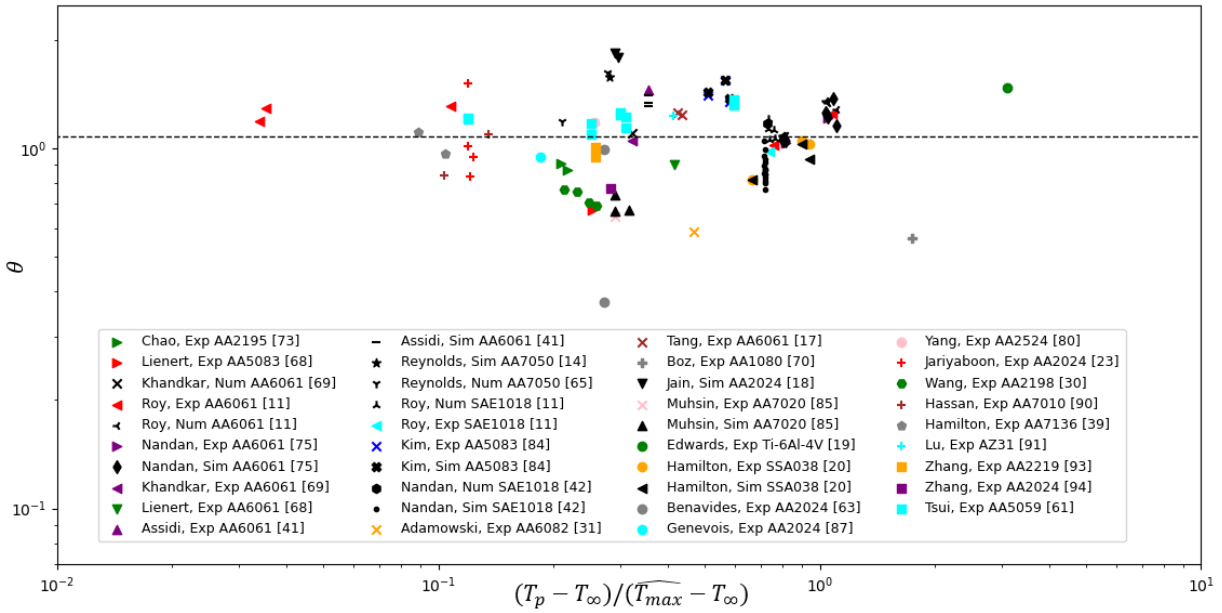

Figure 4.9: Ratio of maximum temperature as a function of $(T_p - T_\infty)/(\widehat{T_{max}} - T_\infty)$. One ε for all materilas.

Using a single ε, the model once more underpredicts the estimation of maximum temperature by slightly less than 7%, meaning that the trendline is closer to 1 for this case. The correction function in this case is given by:

$$f(\widehat{\delta}/a) = 1.075\left(1 + 0.2823\frac{\widehat{\delta}}{a}\right)^{-1.1142} \tag{4.13}$$

As well as in the previous section, the trendlines presented in Figures 4.6, 4.7 and 4.9 correspond to the correction function evaluated at $\widehat{\delta}/a = 0$, because no dependence of Pe, $(T_p - T_\infty)/(\widehat{T_{max}} - T_\infty)$ or $(V/\omega\widehat{\delta})$ in the temperature ratio was observed. Finally, Figure 4.10 presents the correlation between measurement $(T_{max} - T_\infty)$ and improved estimation of the maximum temperature $(\widehat{T_{max}} - T_\infty)^+$ given by Equation 4.12. The graph obtained is very similar to the one in Figure 4.5 as expected.

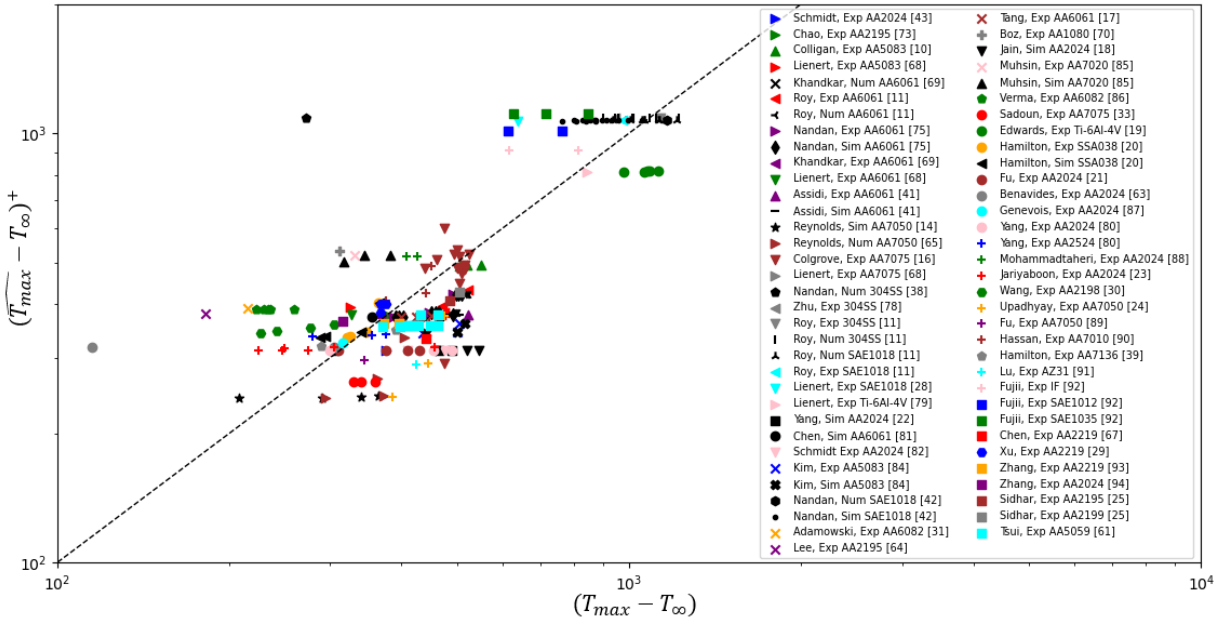

Figure 4.10: Correlation between the maximum temperature reported in the literature and the improved maximum temperature. One ε for all materials.

4.3 Estimation of torque

4.3.1 Ratio of torque, optimizing for every material family.

For these graphs, the values of ε used are the ones optimized from all the experimental points of the data set, separated into groups depending on the family of the material (Table 4.1). Figures 4.11, 4.12, 4.13 and 4.14 present the ratio of torque as a function of the expressions in Equations 4.3 through 4.6. The simplifications are not always satisfied for any of the graphs, but an appropriate amount of points appear on them.

Figure 4.11 and 4.14 present the ratio of torque against the Peclet number (Pe) and $(T_p - T_\infty)/(\widehat{T_{max}} - T_\infty)$. Both graphs present a smaller amount of points compared to graphs in Figure 4.1 and 4.4. Additionally, in Figure 4.11 and 4.14, the amount of points under the trendline is greater than the amount of points above it, nevertheless all points fall around the line, with a significant group of them very close to 1. It is noteworthy that all the points in Figure 4.14 are scattered between 0.2 and 0.6 across the horizontal axis. This can not be observed in the rest of the graphs, as in Figure 4.12, for example, points are scattered through almost 11 orders of magnitude.

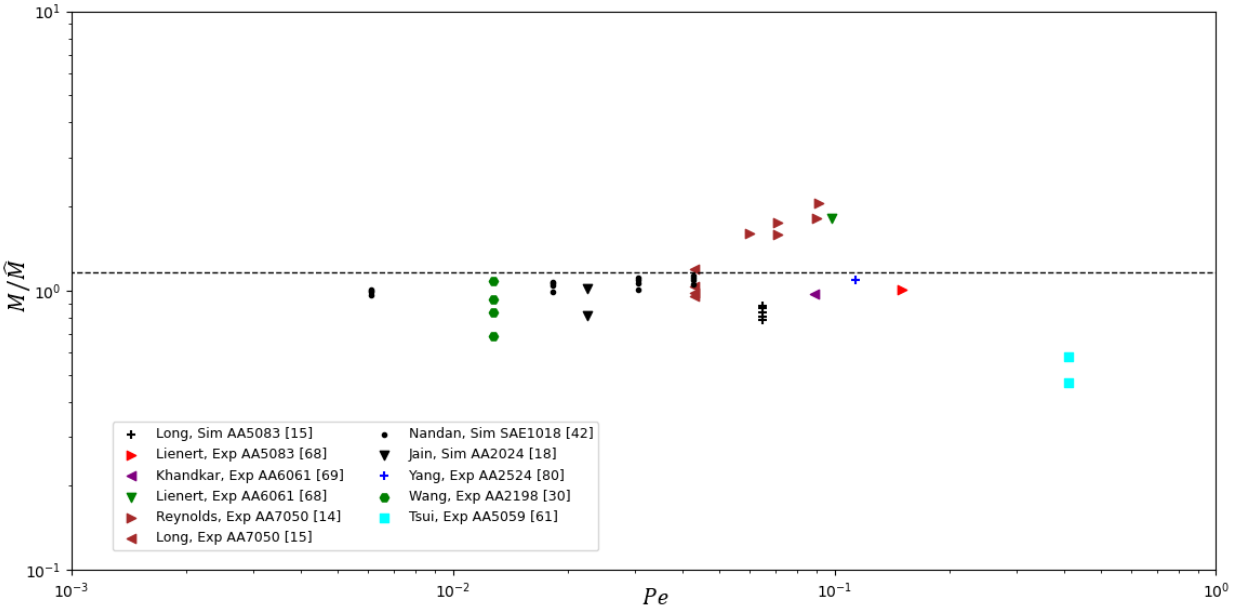

Figure 4.11: Ratio of torque as a function of Peclet Number. Different ε according to material family.

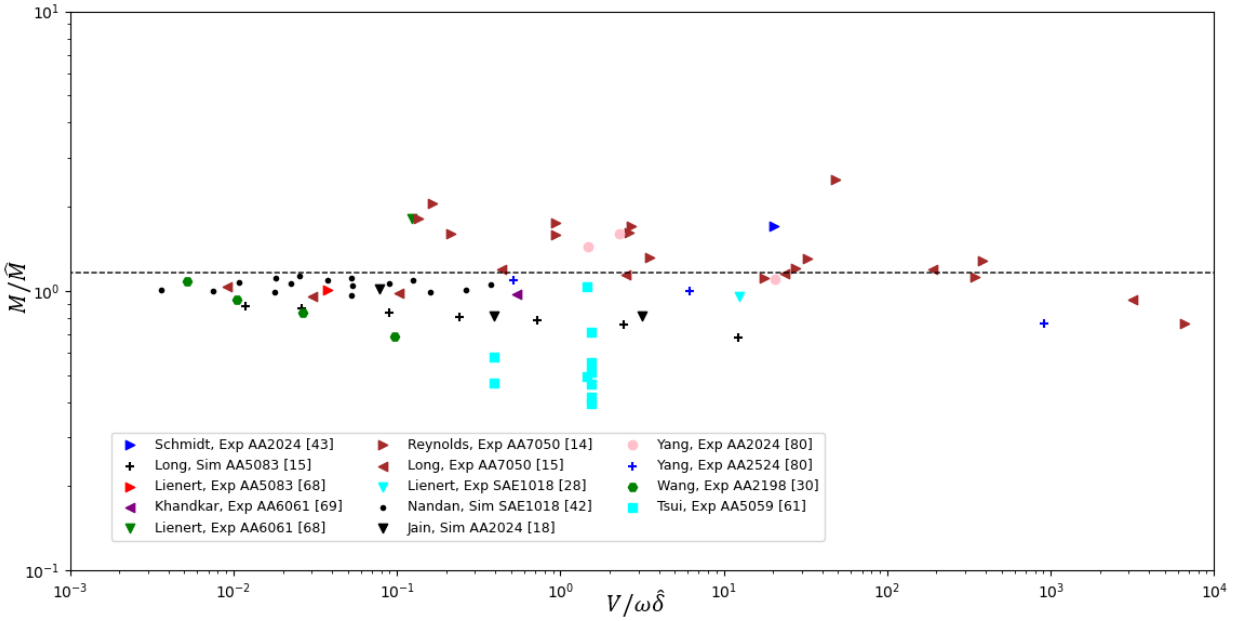

Figure 4.12: Ratio of torque as a function of $(V/\omega\widehat{\delta})$. Different ε according to material family.

Figure 4.12 and 4.13 present the ratio of torque against $(V/\omega\widehat{\delta})$ and $(\widehat{\delta}/a)$. In these graphs, the amount of points under and above the trendline are similar. Once again, in both cases a considerable amount of points are very close to 1, with a few of them from Tsui [61], Reynolds *et al.* [14] and Lienert *et al.* [68] falling away from the trendline and the unitary value. For any of the graphs, no dependence on the simplifications with the estimation of torque can be observed. Because of this, only the constant C_1 is considered for the correction function. The model underpredicts the estimation of torque by approximately 14% with an associated error of 14.326.

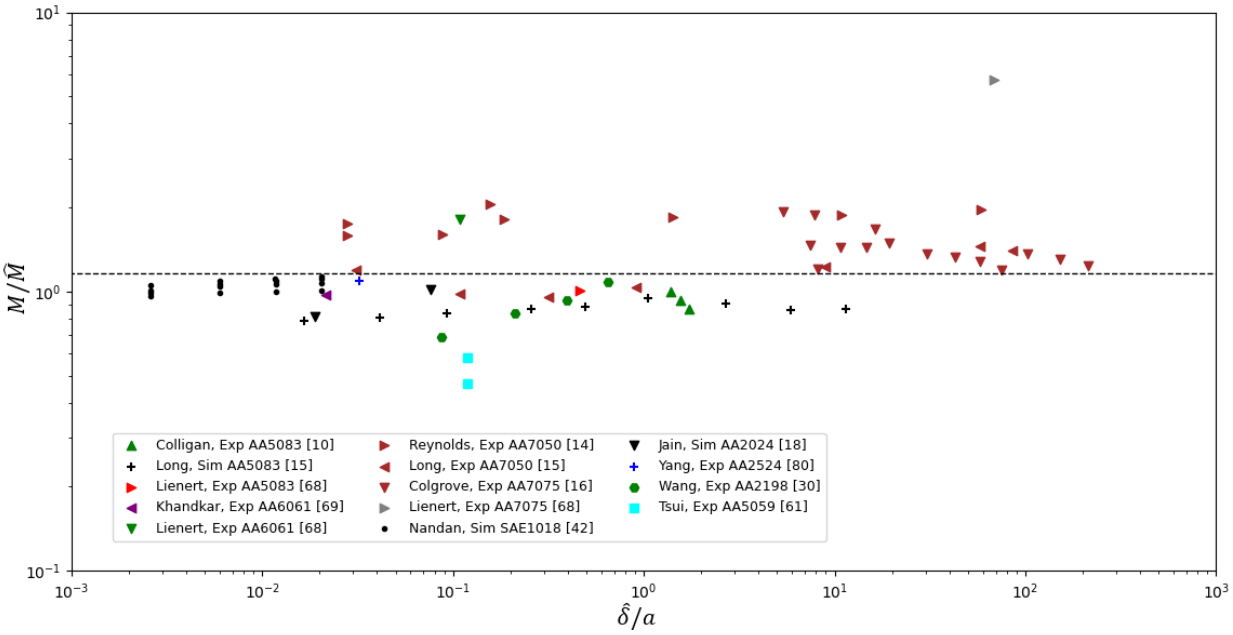

Figure 4.13: Ratio of torque as a function of $(\widehat{\delta}/a)$. Different ε according to material family.

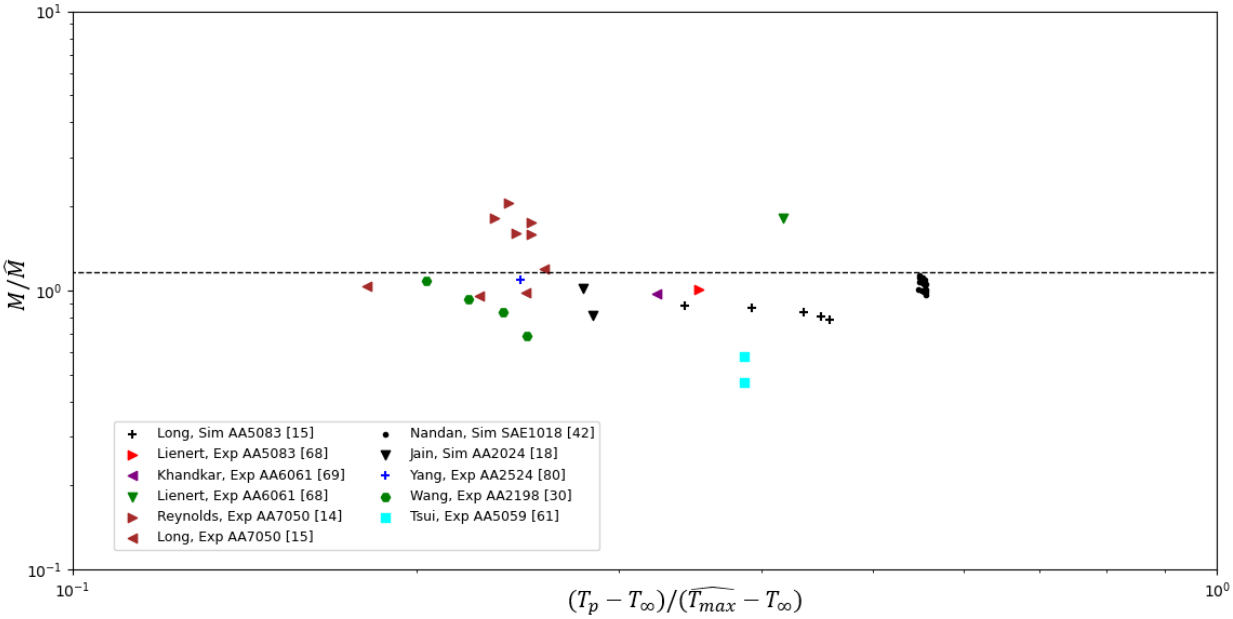

Figure 4.14: Ratio of torque as a function of $(T_p - T_\infty)/(\widehat{T_{max}} - T_\infty)$. Different ε according to material family.

Therefore, the correction function for the estimation of torque is given by:

$$f = 1.162 \tag{4.14}$$

Figure 4.15 presents the correlation between torque measurement (M) and the improved torque estimation $(\widehat{M}^+)$ following Equation 4.15.

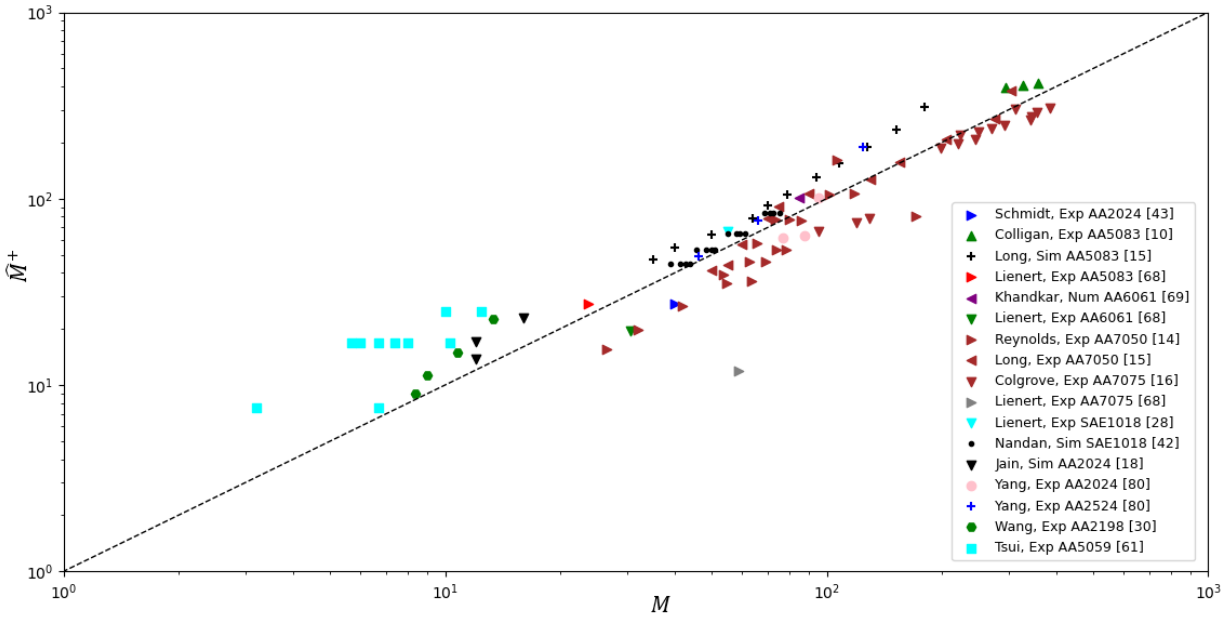

Figure 4.15: Correlation between the torque reported in the literature and the improved torque. Different ε according to material family.

$$\widehat{M}^+ = 1.162\widehat{M} \tag{4.15}$$

Figure 4.15 shows every measurement of torque in the database with a clear orientation around the 1:1 trendline. Besides Lienert *et al.* [68] AA7075 experiment and a few points from Tsui [61], the data seems to respond properly to the estimation improvement.

4.3.2 Ratio of torque, optimizing for all material.

For these graphs, the value of ε is optimized from every material in the data set. This value can be found in Table 4.1 as 'All materials'. Same as before, Figures Figures 4.16, 4.17, 4.18 and 4.19 present the ratio of maximum temperature as a function of the expressions in Equations 4.3 through 4.6.

Figure 4.16 presents the ratio of torque against the Peclet number (Pe). Very few differences can be observed in the graph when comparing it with Figure 4.11. More points from Tsui [61] can be seen and less points from Reynolds *et al.* [14] are present. The points are scattered across the same orders of magnitude through the horizontal axis and, apart from Tsui [61], points seem to be closer together near the trendline. This is confirmed as the error associated to the fitting is equal to 10.404.

Figure 4.19 presents the ratio of torque against $(T_p - T_\infty)/(\widehat{T_{max}} - T_\infty)$. Once again, more points from Tsui [61] can be seen in the graph comparing it with Figure 4.14. The distribution of the points across the horizontal axis is similar, but in this case the main group of points seem to be closer together except for points from Nandan *et al.* [42], that drifted apart, and a couple of points from Tsui [61].

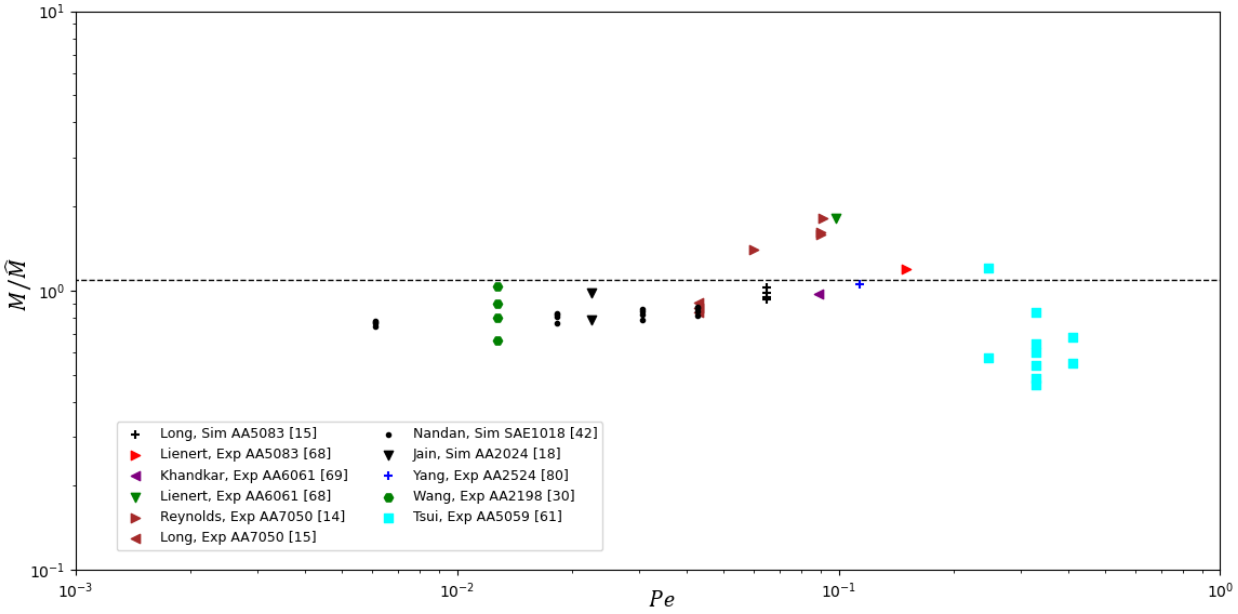

Figure 4.16: Ratio of torque as a function of Peclet Number. One ε for all materials.

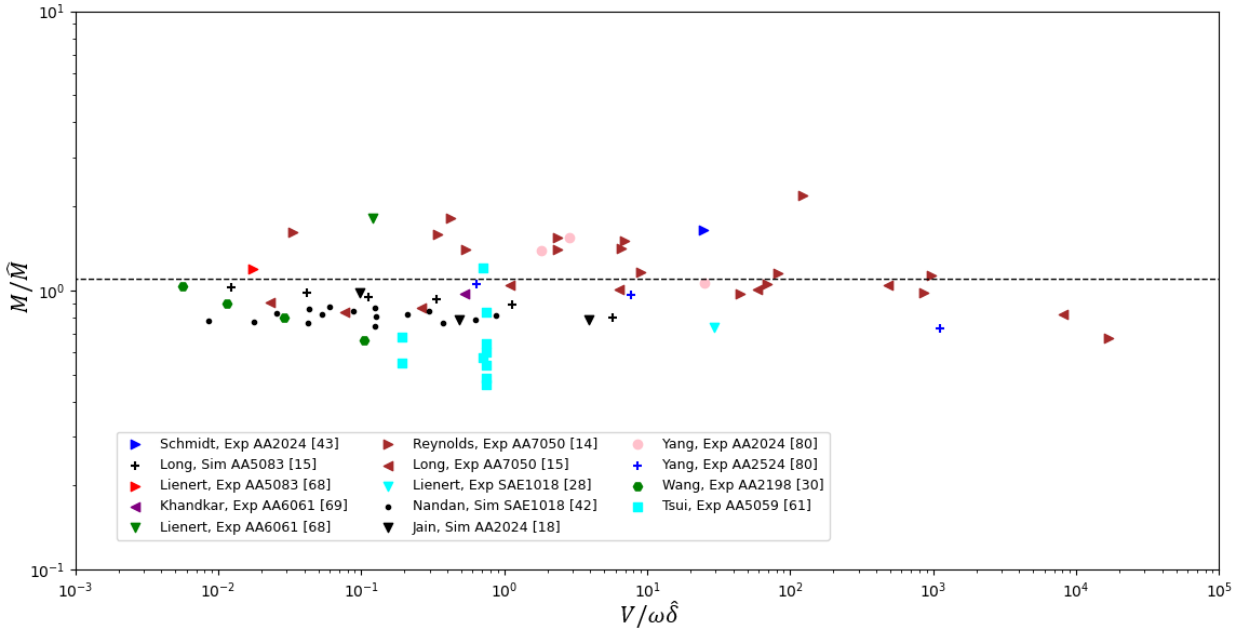

Figure 4.17: Ratio of torque as a function of $(V/\omega\widehat{\delta})$. One ε for all materials.

Figure 4.17 and 4.18 present the ratio of torque against $(V/\omega\widehat{\delta})$ and $(\widehat{\delta}/a)$. Not much differences are noticeable between these graphs and the ones in Figures 4.12 and 4.13. Some points drifted apart through the horizontal axis, which is the case for the scatter in Figure 4.17, and others came closer together, as in the case of Figure 4.18. Additionally, no dependence on the simplifications with the estimation of torque can be observed. However, in this case, the model underpredicts the estimation of torque by approximately 9%. This means that in this case, the points are closer to the objective value.

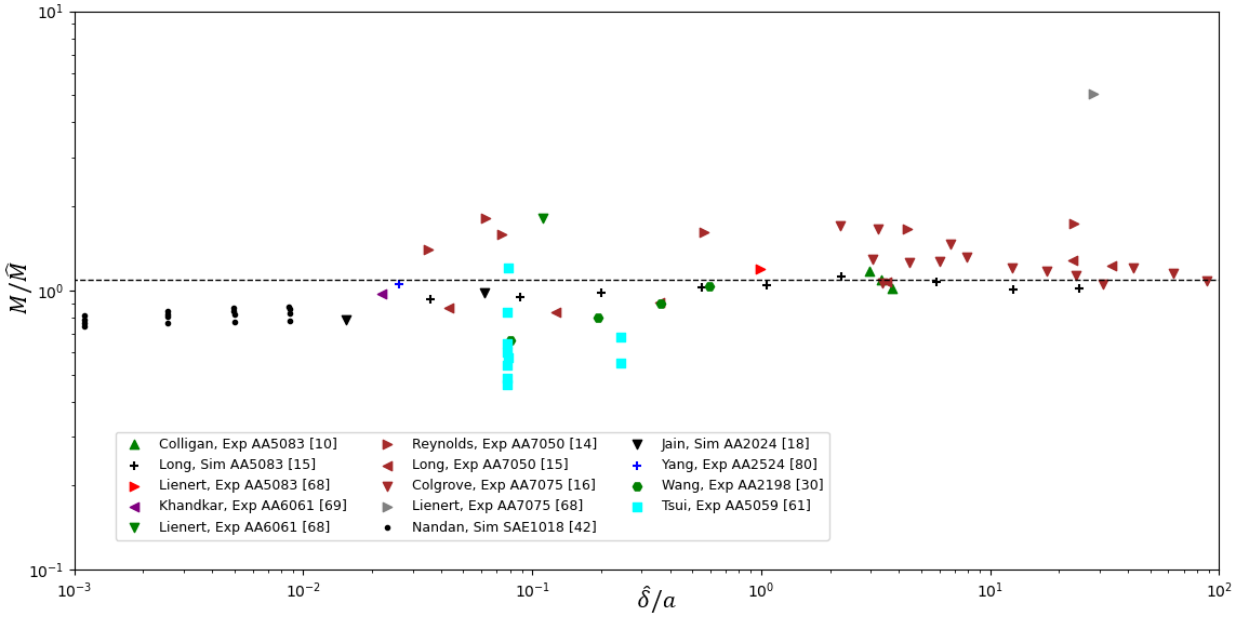

Figure 4.18: Ratio of torque as a function of $(\widehat{\delta}/a)$. One ε for all materials.

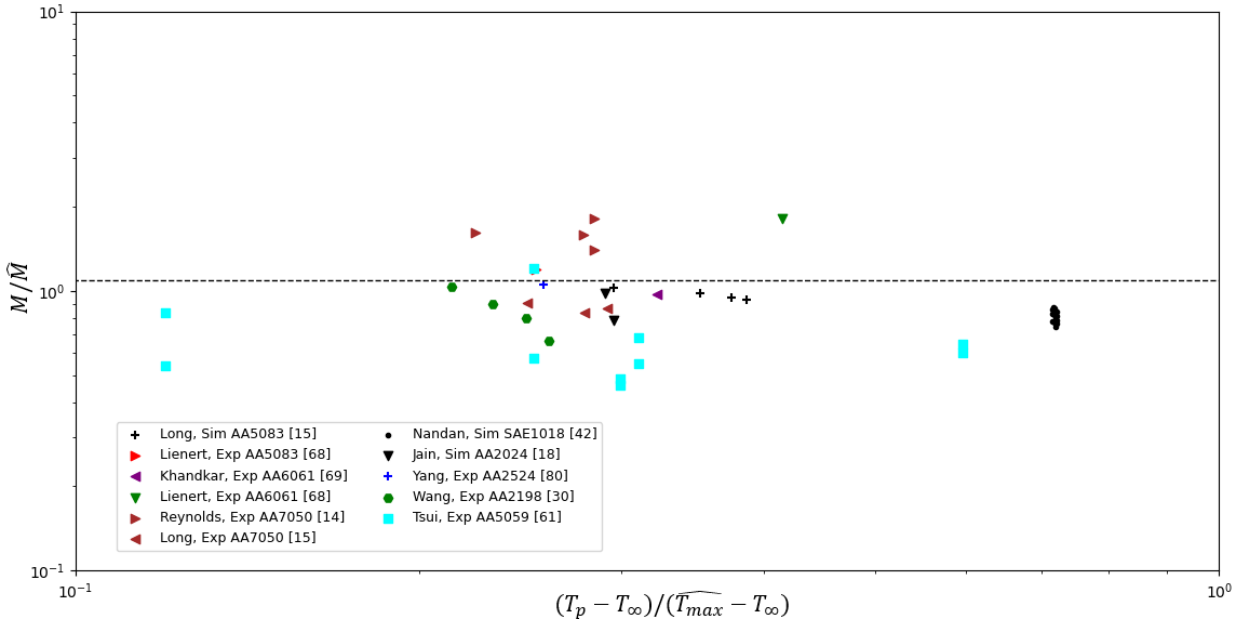

Figure 4.19: Ratio of torque as a function of $(T_p - T_\infty)/(\widehat{T_{max}} - T_\infty)$. One ε for all materials.

Consequently, the correction function for the estimation of torque is given by:

$$f = 1.0959 \tag{4.16}$$

Figure 4.20 presents the correlation between torque measurement (M) and the improved torque estimation $(\widehat{M^+})$ following Equation 4.17.

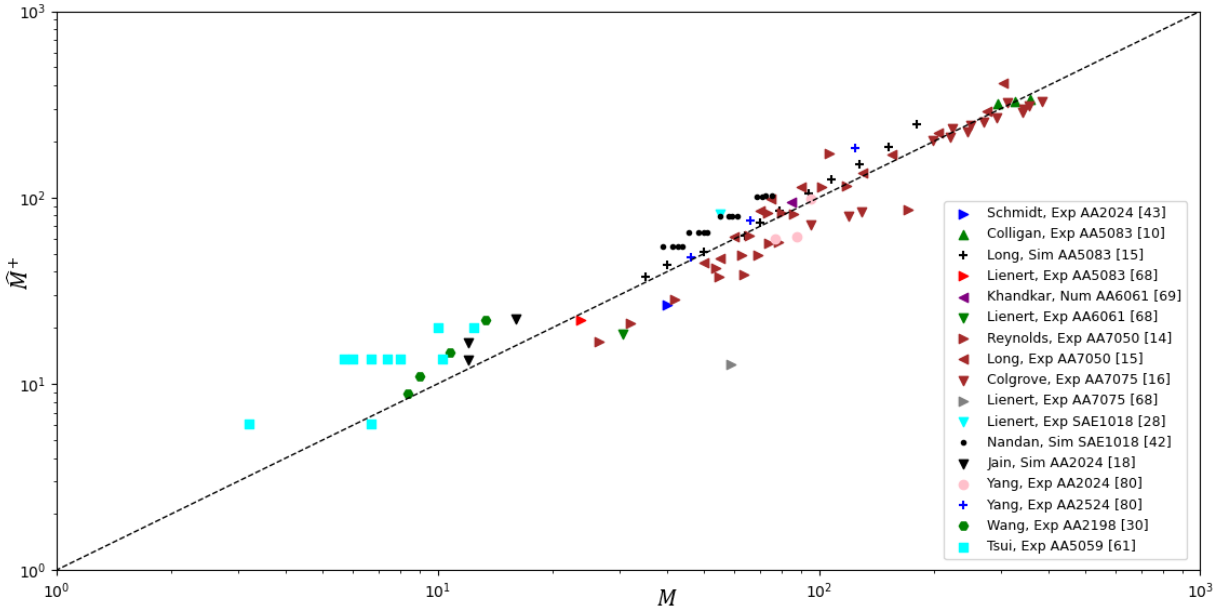

Figure 4.20: Correlation between the torque reported in the literature and the improved torque. One ε for all materials.

$$\widehat{M}^+ = 1.0959\widehat{M} \tag{4.17}$$

Figure 4.20 shows every measurement of torque in the database with a clear orientation around the 1:1 trendline. Once again, besides Lienert *et al.* [68] AA7075 experiment and a few points from Tsui [61], the data seems to respond properly to the estimation improvement and even better than in Figure 4.15 as they are closer to the trendline.

4.4 Ratio of Torque considering shoulder effect

As it was mentioned in the beginning of this section, the estimation of torque ($\widehat{M}$) used for the ratio in the graphs was the one given by Equation 2.51. This estimation considers only the torque generated by the pin, disregarding the torque generated by the shoulder. Mendez *et al.* [2] proposed a solution in his paper where torque generated by the pin is considered.

The torque due to the shoulder action is given by:

$$\widehat{M}_s = \int_a^b \int_0^{2\pi} \tau(r,\theta) r^2 dr d\theta \tag{4.18}$$

where $\tau(r,\theta)$ is the shear stress in the circumferential direction the substrate transmits to the shoulder surface. To evaluate this integral applying scaling analysis, the shear stress can be expressed as:

$$\tau(r,\theta) = \tau_c - \Delta\tau\tau^* \tag{4.19}$$

where τ_c is the same characteristic value as for the shear layer, τ^* is the dimensionless counterpart of $\tau(r,\theta)$, and $\Delta\tau = \tau_{min} - \tau_{max}$ scales the variations in shear stress. It is important to mention that in Equation 4.19, the minus sign is present because variations in the FSW process, such as tool inclination angles, tend to decrease shear stress in the front part of the shoulder. Another example occurs when there are transitions of sticking to sliding conditions. Additionally, the sheared region by the pin decreases the shear forces experienced by the shoulder. Considering this, Equation 4.18 can be expressed as:

$$\widehat{M_s} = f\frac{2}{3}\,\pi\,\widehat{\tau_c}\,(b^3 - a^3) \tag{4.20}$$

where

$$f = 1 - \frac{\Delta\tau}{\widehat{\tau_c}}\frac{\int_a^b\int_0^{2\pi}\tau^* r^2 dr d\theta}{\frac{2}{3}\pi(b^3-a^3)} \tag{4.21}$$

The torque factor f is expected to relate to the plunging force of the tool, being smallest for small plunge forces, and saturating to a constant value for large plunge forces. The preheat temperature expected from the action of the shoulder can then be calculated using Equation PPP. Finally, the torque estimation is given by the following equation:

$$\widehat{M} = \widehat{M_p} + \widehat{M_s} = 2\pi\widehat{\tau_c}a^2 d\left\{1 + \frac{f}{3}\frac{a}{d}\left(\left(\frac{b}{a}\right)^3 - 1\right)\right\} \tag{4.22}$$

4.4.1 Ratio of torque graphs considering shoulder effect

For these graphs, the value of ε is optimized from every material in the data set. This value can be found in Table 4.1 as 'All materials'. Same as before, Figures 4.21, 4.22, 4.23 and 4.24 present the ratio of maximum temperature as a function of the expressions in Equations 4.3 through 4.6.

When comparing the graphs in 4.21, 4.22, 4.23 and 4.24 with the ones in Section 4.3.2, the main difference is that all the points drifted to a lower part of the graph, carrying the trendline to a point lower than 1. Because of this, the model overpredicts the estimation of torque by nearly 30% with an associated error of 9.052. In this case, the correction function is given by Equation 4.23. This behavior is somewhat expected because when the estimation of torque considers only the effect of the pin, the trendline is already near 1. In consequence, when another value is added to the estimation, the model will tend to overpredict the torque value expected.

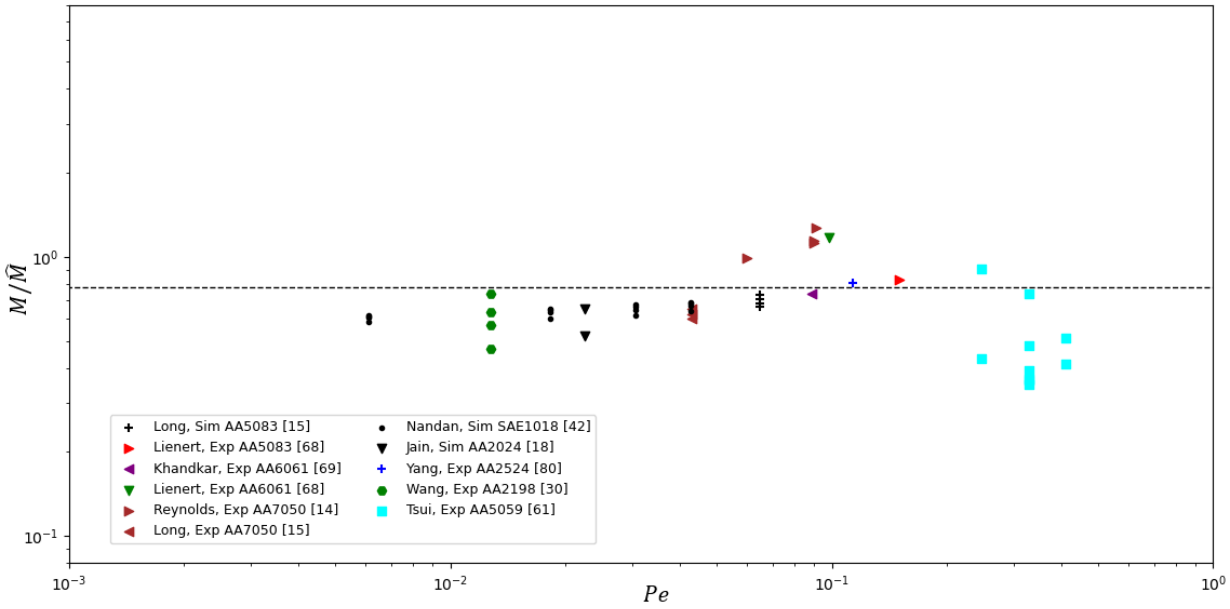

Figure 4.21: Ratio of torque considering shoulder effect as a function of Peclet Number. One ε for all materials.

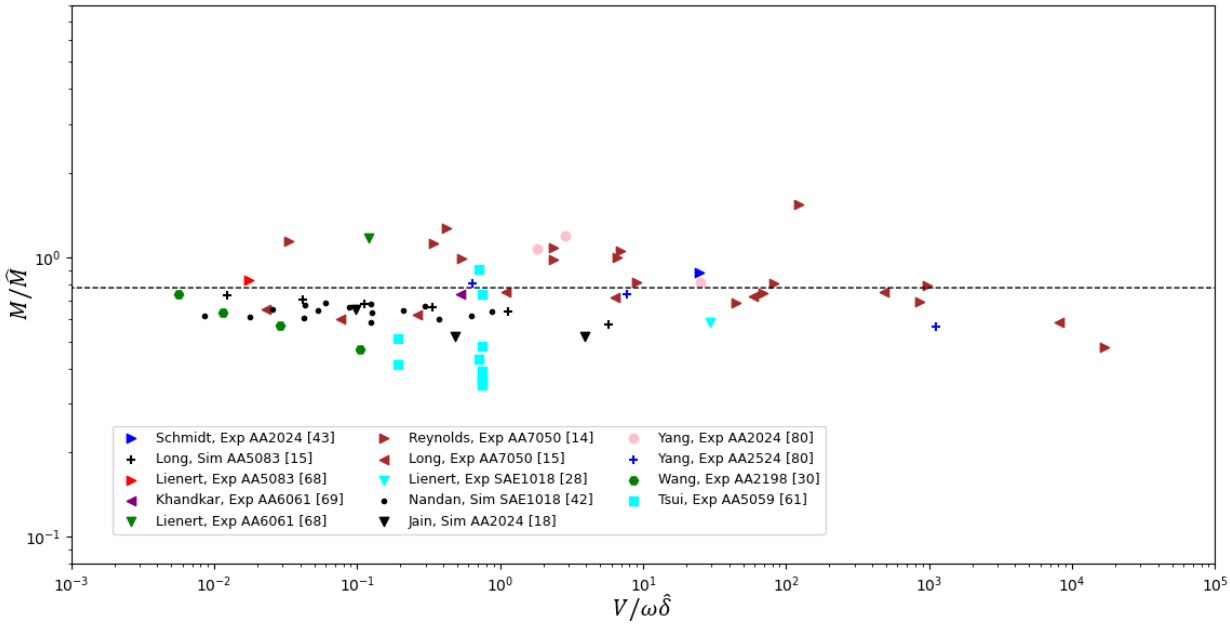

Figure 4.22: Ratio of torque considering shoulder effect as a function of $(V/\omega\widehat{\delta})$. One ε for all materials.

$$f = 0.7773 \tag{4.23}$$

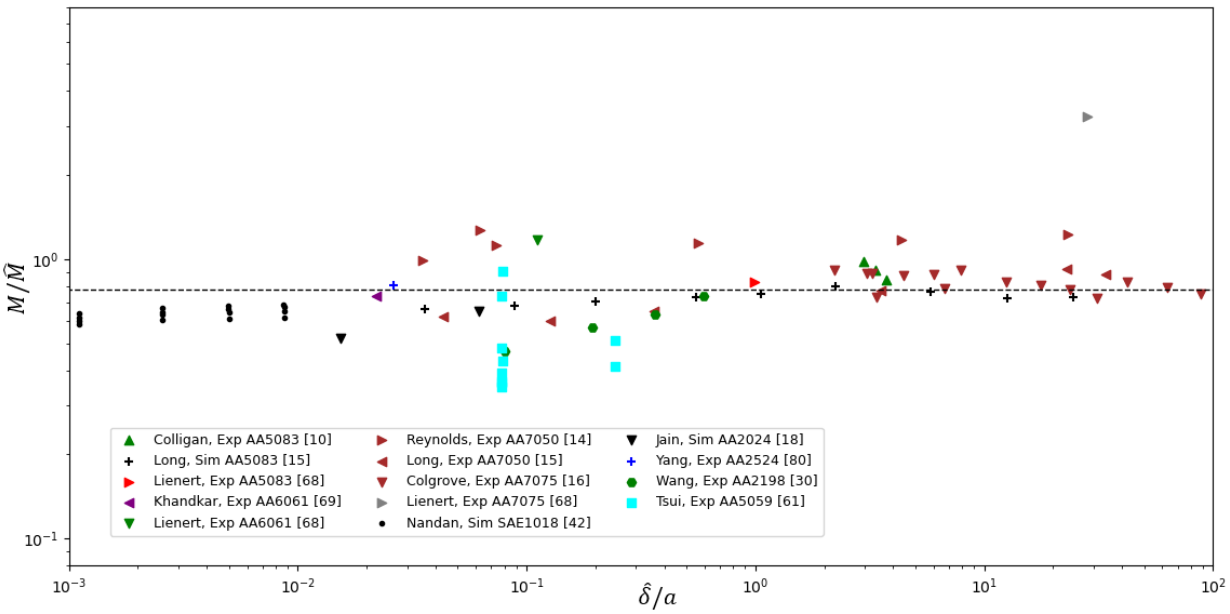

Figure 4.23: Ratio of torque considering shoulder effect as a function of $(\widehat{\delta}/a)$. One ε for all materials.

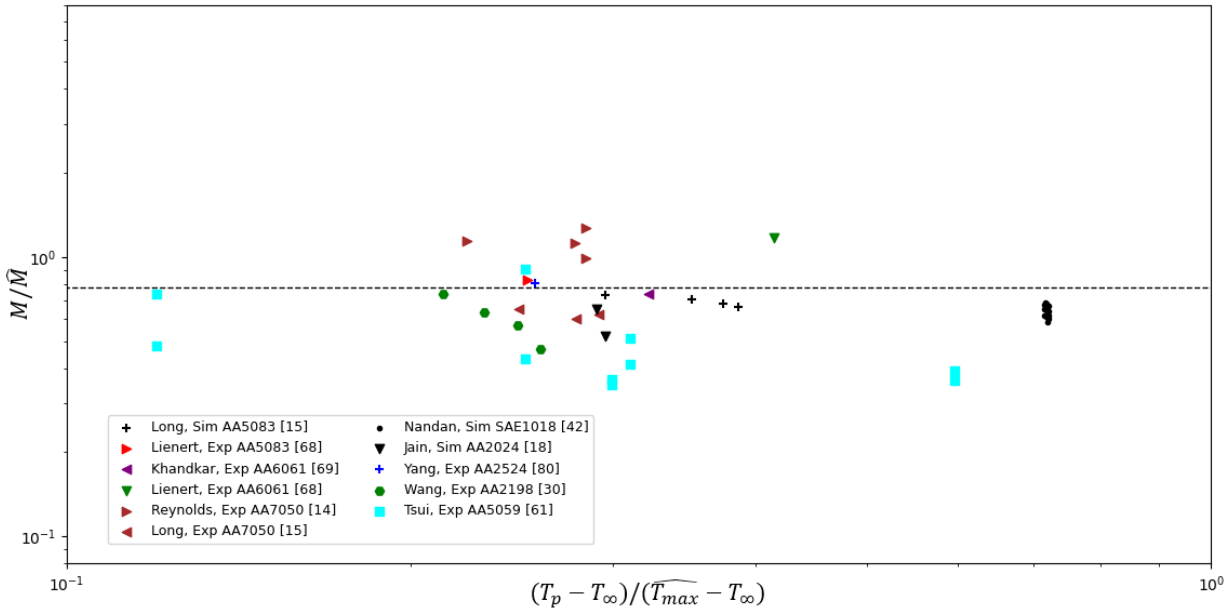

Figure 4.24: Ratio of torque considering shoulder effect as a function of $(T_p - T_\infty)/(\widehat{T_{max}} - T_\infty)$. One ε for all materials.

Chapter 5

Discussion

The new considerations have improved the results previously obtained by earlier developments in the model, where a temperature gradient was not considered near the pin [2]. Even when new data was added to the existing database, some of which considered new materials, both maximum temperature estimations and torque estimations presented better results. Furthermore, the model continues to work regardless of the material of the work-piece, which is one of the main advantages of this thermomechanical approach. New aluminum alloys, new steels and a magnesium alloy behaved as expected. This is due to the fact that the estimations depend on parameters of the process, material properties and work-piece/tool dimensions, without relying on any empirical data.

The value of ε takes a relevant role in this work and, by extension, in the model. This acts as an auxiliary variable and, although its physical significance is not completely clear, the optimizations work correctly when searching for estimations closer to the values expected. However, some counterintuitive results were obtained. This is because the optimization of ε done considering all the materials got better results than the optimization done per material family. Comparing the results, Equation 4.13 shows a slightly better behavior for the ratio of maximum temperature than Equation 4.11, as the trendline is closer to 1. On the other hand, estimations of torque present a more significant improvement as the torque ratio is approximately 5% closer to the expected value.

Since it is not completely clear what ε represents in a physical sense, it becomes difficult to generate hypothesis that may explain why the estimations get better or worse as this value changes. It is important to note that, the calculations on ε depend on the relationship between T_{sol} and T_{δ} through the Arrhenius behavior of $\dot{\gamma_{sol}}$ and $\dot{\gamma}_{\delta}$ represented in Figure 2.5. In other words, the material dictate the behavior of ε. Due to this, it was not expected that the estimations done with a unique value of ε performed better than the other case, where ε was optimized for each material family. Nevertheless, ε shows to have significant physical meaning that future research must explore.

Different possibilities can be proposed as to why better results are obtained when one optimized value of ε is used. One of the possibilities is that the experimental errors of the real FSW tests present in the database are carried through the calculations and represented by this phenomenon. Also, someone could argue that since for some of the materials the constants for the calculations of the constitutive model could not be found in the literature and data of similar materials was used, this could have tampered the results. However this last one is unlikely because, once again, the constants sheared between materials are from similar characteristics and same material family, the same considered in the ε optimizations.

Considering the above, the results point to a much simpler explanation. Looking at the graphs from Figure 4.1 through 4.4 and Figure 4.11 through 4.14, when different values of ε are considered, the points seem to scatter further away from the trendline across the vertical axis. This is confirmed as the fit error is always lower when the estimations (of maximum temperature ratio and torque ratio) are done using a single optimized value of ε. Although this does not explain why the results are better when one optimized value of ε is used, it opens up the possibility that a group of points increased in value, which could explain why the trendline drifts away form 1 when different values of ε are considered. This could also mean that, for some particular points the results are better when different values of ε are used on different material families. This is exactly the case for Nandan *et al.* [42], where the points in Figure 4.17 are around 0.8, in Figure 4.12 are much closer to 1.

Another noteworthy result in this work is torque estimations. It was already mentioned in Chapter 4 that the torque estimations used for the graphs in Figures 4.11 through 4.19 considers only the torque generated by the pin, dismissing the torque generated by the shoulder. Not taking into account the torque generated by the shoulder implies ignoring an important part of the physics involved in FSW. However, the results obtained considering only the effect of the pin are very promising and the ratio between the experimental values and the estimations are very close to 1. Not so for when the shoulder effect is considered, as torque is overpredicted by nearly 30%. The reason behind this is quite straightforward. The behavior of the work-piece considered for the constitutive model is a tangent line to the curve of $\dot{\gamma}/\gamma_m$ as a function of temperature (see Figure 2.5). To correct this situation, a secant line must be consider, this way calculations are compensated and shoulder effects are taken into account.

Within the graphs, interesting analysis, comparisons and conclusions can be deduced. Simulation and numerical points seem to have a similar behavior to experimental points. In Figure 4.14, the torque ratio for Jain *et al.* [18] and Nandan *et al.* [42] simulations on AA2024 and SAE1018 are very close to Wang *et al.* [30] and Long *et al.* [15] experimental tests on AA2198 and AA7050. And in Figure 4.6, the temperature ratio for Nandan *et al.* [42] simulations on SAE1018 is fairly close to Roy *et al.* [11] experimental points on the same material. In the same graph, points from Hamilton *et al.* [20] appear to be nearly the same for experimental and simulation runs on SSA038 aluminum. This last comparison suggests that the data obtained by the simulation done by Hamilton *et al.* [20] is very close to the real experiment.

No particular material seems to work better or worse according to the graphs in Chapter 4. For example, in Figure 4.4, Assidi *el al.* [41] and Khandkar *et al.* [69] experimental points are on the same AA6061 aluminum alloy and the second is much closer to 1 than the first one. When comparing between materials, no conclusions can be drawn either. Comparing, for example, aluminum alloy AA2024 with SAE1018 steel experimental tests in Figure 4.7, both materials present points very close to 1 (Jariyaboon *et al.* [23], Roy *et al.* [11]) and others not as good (Benavides *et al.* [63], Lienert *et al.* [28] and Nandan *et al.* [42]). Additionally, there are materials that present a very few amount of points. This is because the simplifications were not satisfied or there are very few data on those particular materials. This is the case of Ti-6Al-4V, AZ31 and a couple of aluminum alloys. For those materials, though they seem to respond well to the model, no conclusions can be made.

Following graphs analysis, there are some points that do not follow the trendline as the vast majority do. One clear example is a point from Benavides *et al.* [63] in all maximum temperature ratio graphs. This particular point has a ratio of about 0.37 (for one or different values of ε). It is far from other points of the same aluminum alloy and even another point from the same paper. This is because in the source where this points are taken from, the authors are testing FSW welds on materials at room temperature and low temperature. The point far from the trendline comes from a test where the material is cooled up to -30°C with liquid nitrogen. Even if a T_∞ equal to 233K (-30°C) is considered, the ratio of maximum temperature comes to a value of 0.49, far from 1. But what stands out is that, the weld at room temperature (the point from Benavides *et al.* [63] that is close to 1 in the temperature ratio graphs) presents virtually no defects, whereas the weld at low temperature presents a significant tunnel defect. This is a very positive result for the model as faulty welds have bad results and defect-free welds behave as expected.

Other points that stand out are from Adamowski *et al.* [31] and Boz *et al.* [70] in Figures 4.6 and 4.9. In the case of Adamowski *et al.* [31], the author reported some tunnel defects and Boz *et al.* [70] stated that the pin used retained material during the tests and the calibration of the parameters depended on this phenomenon. In torque ratio graphs, there is one point from Lienert that stands out (see Figures 4.13 and 4.18). The ratio registered by this point is approximately 5. This high discrepancy comes from the high rotational speed of the test. Nearly three times faster than other tests for the same material. This is reflected in the estimation of torque as the shear stress decreases significantly and so does torque (see Equation 2.51). Only when the effect of the shoulder is considered in the estimation of torque, the ratio drops to around 3.2 (see Figure 4.23). This is because the estimation is higher as shoulder effect is considered.

Finally, it is worth noticing the wide range where points are scattered across the horizontal axis in some graphs. Coincidentally, those graphs are the ones with the simplifications that include the delta estimation $\widehat{\delta}$. This estimation could be the responsible for this orders of magnitude differences. As Equation 2.47 states, $\widehat{\delta}$ depends on several values, being A, B', ω and ΔT_δ the main ones that can produce this differences. An interesting exercise could be comparing the estimation of the shear layer $\widehat{\delta}$ with real shear layer thickness. This was done on previews iterations of the model but was dropped as accurate measurements of the shear layer are complicated and too speculative.

Chapter 6

Conclusion

A coupled model of heat transfer and plastic deformation in FSW has been produced using scaling analysis. For this model, new considerations were taken into account as the temperature profile of the work-piece near the pin considers a temperature gradient that account for heat loss through the tool (Figure 2.3). The model generated modified closed-form expressions for the thickness of the shear layer (Equation 2.47), the maximum temperature (Equation 2.48) the volumetric heat generation (Equation 2.49) and the shear stress in the metal (Equation 2.50). The expressions depend only of process parameters and do not depend on any empirical data.

Published data was compared with estimations of maximum temperature and torque calculated using the model. Improvements compared to past iterations of the model were achieved as maximum temperature was underpredicted by 7% and torque was underpredicted by 9%. A comparison was carried out between two ways of applying the auxiliary variable ε, a unique ε optimized from all materials or ε optimized for every material family. Better general results were obtained using a unique ε, however some of the data showed better results when an ε was optimized for a particular material family.

Another comparison done in this work was regarding the estimation of torque. Due to the shape of the FSW tool, torque generates through the effect of the pin and the shoulder. The results in this work considered only the effect of the pin. However, as not considering the effect of the shoulder implies ignoring some of the physics of the problem, estimations of torque including both effects were implemented. The results showed an overprediction of nearly 30%. This was expected as the previous results were very close to 1 and, additionally, the calculations for the constitutive model consider only the effect of the pin.

In the graphs, points followed regularly the trendlines. Although the presence of exceptions is inevitable with a substantial database such as the one used in this work, most of the inconsistencies could be justified as faulty FSW welds or parameter derived disparity. Moreover, the experiments from published data carry errors that inevitably will show in the results as either scatter or discrepancy.

Correction functions were applied to the results of maximum temperature and torque ratios. The correction function makes up for physics disregarded in the model and the mathematical errors induced by the simplifications of the scaling analysis. Improvements were observed for maximum temperature and torque ratio considering both scenarios for the ε value. Estimations fell into the expected values however, as it was already mentioned, scatter was always present.

Finally, as this investigation shows, welding parameters are key for designing a successful FSW weld. Material properties and tool settings determine the maximum temperature of the work-piece during the process which is arguably the most important magnitude in FSW. Other magnitudes like the shear stress, torque and shear layer dimensions constitute an important part of the process too. Therefore, this modification to a previously proposed model can be of great help for future FSW tests, providing guidance for the parameters setting for a particular material. The model is close to predict, without any experimentation involved, key values to perform successful FSW welds. Future scopes of this work include adjusting the equations of torque estimation considering the shoulder effect and defining a value of the auxiliary variable ε that works best for the model.

Bibliography

[1] Akshansh Mishra. Friction Stir Welding of Dissimilar Metal: A Review. *International Journal for Research in Applied Science & Engineering Technology (IJRASET)*, 6(1):1551–1559, 2018.

[2] Patricio Mendez, Karem Tello, and Thomas Lienert. Scaling of coupled heat transfer and plastic deformation around the pin in friction stir welding. *Acta Materialia*, 2009.

[3] Thomas W.M., Nicholas E.D., Needham J.C., Murch M.G., Temple-Smith P., and Dawes C. J. Friction stir butt welding. GB patent no.9125978.8, 1991.

[4] Nilesh Kumar, Wei Yuan, and Rajiv S. Mishra. *Friction Stir Welding of Dissimilar Alloys and Materials*. Elsevier, Oxford, 1 edition, 2015.

[5] Naiyi Li, Tsung-Yu Pan, Ronald P. Cooper, Dan Q. Houston, Zhili Feng, and Michael L. Santella. Friction stir welding of magnesium AM60 alloy. *TMS (The Minerals, Metals & Materials Society)*, 2004.

[6] Walter Polt. A little friction at Boeing. *Boeing Frontiers*, 3(5), 2004.

[7] Fred Delany, Stephan W. Kallee, and Mike J Russell. Friction stir welding of aluminium ships. *International Forum on Welding Technologies in the Shipping Industry (IFWT)*, 2007.

[8] R. Nandan, T. DebRoy, and H.K.D.H. Bhadeshia. Recent advances in friction-stir welding process, weldment structure and properties. *Progress in Materials Science*, 2008.

[9] Xiaocong He, Fengshou Gu, and Andrew Ball. A review of numerical analysis of friction stir welding. *Progress in Materials Science*, 2014.

[10] Kevin Colligan. Relationships between process variables related to heat generation in FSW of aluminum. *TMS (The Minerals, Metals and Materials Society)*, 2007.

[11] G.G. Roy, R. Nandan, and T. DebRoy. Dimensionless correlation to estimate peak temperature during friction stir welding. *Science and Technology of Welding and Joining*, 2006.

[12] Shaowen Xu and Xiaomin Deng. A study of texture patterns in friction stir welds. *Acta Materalia*, 2008.

[13] H. Atharifar, D.C. Lin, and R. Kovacevic. Studying Tunnel-like Defect in Friction Stir Welding Process Using Computational Fluid Dynamics. *Numerical, Mathematical, and Physical Modelling Tools for Materials Processes II*, 2007.

[14] A.P. Reynolds, Z. Khandkar, T. Long, W. Tang, and J. Khan. Utility of relatively simple models for understanding process parameter effects of FSW. *Materials Science Forum*, 2003.

[15] T. Long, W. Tang, and A. P. Reynolds. Process response parameter relationships in aluminium alloy friction stir welds. *Science and Technology of Welding and Joining*, 2007.

[16] P.A. Colegrove and H. R. Shercliff. Experimental and numerical analysis of aluminium alloy 7075-T7351 friction stir welds. *Science and Technology of Welding and Joining*, 2003.

[17] W. Tang, X. Guo, J.C. McClure, and L.E. Murr. Heat input and temperature distribution in friction stir welding. *Journal of Materials Processing and Manufacturing Science*, 1999.

[18] Rahul Jain, Surjya K. Pal, and Shiv B. Singh. A study on the variation of forces and temperature in a friction stir welding process: A finite element approach. *Journal of Manufacturing Processes*, 2015.

[19] P. Edwards and M. Ramulu. Peak temperatures during friction stir welding of Ti–6Al–4V. *Science and Technology of Welding and Joining*, 2010.

[20] C. Hamilton, A.Sommers, and S.Dymek. A thermal model of friction stir welding applied to Sc-modified Al–Zn–Mg–Cu alloy extrusions. *International Journal of Machine Tools and Manufacture*, 2008.

[21] Rui dong Fu, Jian feng Zhang, Yi jun Li, Ju Kang, Hui jie Liu, and Fu cheng Zhang. Effect of welding heat input and postwelding natural aging on hardness of stir zone for friction stir-welded 2024-T3 aluminum alloy thin-sheet. *Materials Science and Engineering A*, 2012.

[22] Bangcheng Yang, Junhui Yan, Michael A. Sutton, and Anthony P. Reynolds. Banded microstructure in AA2024-T351 and AA2524-T351 aluminum friction stir welds. *Materials Science and Engineering A*, 2004.

[23] M. Jariyaboon, A.J. Davenport, R. Ambat, B.J. Connolly, S.W. Williams, and D.A. Price. The effect of welding parameters on the corrosion behavior of friction stir welded AA2024-T352. *Corrosion Science*, 2007.

[24] P. Upadhyay and A.P. Reynolds. Effects of thermal boundary conditions in friction stir welded AA7050-T7 sheets. *Materials Science and Engineering A*, 2009.

[25] Harpreet Sidhar and Rajiv S. Mishra. Aging kinetics of friction stir welded Al-Cu-Li-Mg-Ag and Al-Cu-Li-Mg alloys. *Materials and Design*, 2016.

[26] R.W. Fondaa and J.F. Bingert. Texture variations in an aluminum friction stir weld. *Scripta Materalia*, 2007.

[27] M. Guerra, C. Schmidt, J.C. McClure, L.E. Murr, and A.C. Nunes. Flow patterns during friction stir welding. *Materials Characterization*, 2003.

[28] T.J. Lienert, W.L. Stellwag, B.B. Grimmet, and R. W. Warke. Friction stir welding studies on mild steel. *The Welding Journal*, 2003.

[29] Weifeng Xu, Jinhe Liu, Guohong Luan, and Chunlin Dong. Temperature evolution, microstructure and mechanical properties of friction stir welded thick 2219-O aluminum alloy joints. *Materials and Design*, 2008.

[30] F.F. Wang, W.Y. Li, J. Shen, S.Y. Hub, and J.F. dos Santos. Effect of tool rotational speed on the microstructure and mechanical properties of bobbin tool friction stir welding of Al-Li alloy. *Materials and Design*, 2015.

[31] J. Adamowski and M. Szkodo. Fsw of AW6082. *Journal of Achievements in Materials and Manufacturing Engineering*, 2006.

[32] A. K. Shukla and W. A. Baeslack. Study of process/structure/property relationships in friction stir welded thin sheet Al–Cu–Li alloy. *Science and Technology of Welding and Joining*, 2009.

[33] A.M. Sadoun, A. Wagih, A. Fathy, and A.R.S. Essa. Effect of tool pin side area ratio on temperature distribution in friction stir welding. *Results in Physics*, 2019.

[34] Axel Fehrenbacher, Neil A. Duffie, Nicola J. Ferrier, Frank E. Pfefferkorn, and Michael R. Zinn. Effects of tool–workpiece interface temperature on weld quality and quality improvements through temperature control in friction stir welding. *The International Journal of Advanced Manufacturing Technology*, 2014.

[35] Liu H, Fulii H, Maeda M, and Nogi K. Tensile properties and fracture locations of friction-stir welded joints of 6061-T6 aluminium alloy. *J Mater Sci Lett*, 2003.

[36] Lee WB, Lee CY, Chang WS, Yeon YM, and Jung SB. Microstructural investigation of friction stir welded pure titanium. *Mater Lett*, 2005.

[37] M. Song and R. Kovacevic. Thermal modeling of friction stir welding in a moving coordinate system and its validation. *International Journal of Machine Tools and Manufacture*, 2003.

[38] R. Nandan, G. G. Roy, T. J. Lienert, and T. DebRoy. Numerical modelling of 3D plastic flow and heat transfer during friction stir welding of stainless steel. *Science and Technology of Welding and Joining*, 2006.

[39] C. Hamilton, S. Dymek, I. Kalemba, and M. Blicharski. Friction stir welding of aluminium 7136-T76511 extrusions. *Science and Technology of Welding and Joining*, 2008.

[40] D.M. Neto and P. Neto. Numerical modeling of the friction stir welding process: a literature review. *Department of Mechanical Engineering, University of Coimbra*, 2009.

[41] Mohamed Assidi, Lionel Fourment, Simon Guerdoux, and Tracy Nelson. Friction model for friction stir welding process simulation: Calibrations from welding experiments. *International Journal for Machine Tools and Manufacture*, 2009.

[42] R. Nandan, G.G. Roy, T.J. Lienert, and T. Debroy. Three-dimensional heat and material flow during friction stir welding of mild steel. *Acta Materalia*, 2006.

[43] H Schmidt, J Hattel, and J Wert. An analytical model for the heat generation in friction stir welding. *Modelling and simulation in materials science and engineering*, 2003.

[44] P. Ulysse. Three-dimensional modeling of the friction stir welding process. *International Journal of Machine Tools and Manufacture*, 2002.

[45] D. Rosenthal. The theory of moving sources of heat and its application to metal treatments. *Transactions of the A.S.M.E.*, 1946.

[46] Mohammad Bagher Nasiri and Norbert Enzinger. An analytical solution for temperature distribution in fillet arc welding based on an adaptive function. *Welding in the world*, 2018.

[47] William M. Deen. Analysis of transport phenomena. *Oxford University Press*, 1998.

[48] J. A. Dantzig and Charles L. Tucker. Modeling in materials processing. *Cambridge University Press*, 2001.

[49] L. A. Segel. Simplification and Scaling. *SIAM Review*, 1972.

[50] L. A. Segel. Advanced Scaling Techniques for the Modeling of Materials Processing. *SIAM Review*, 1972.

[51] ASM International. *ASM Handbook Volume 01: Properties and Selection: Irons, Steels, and High-Performance Alloys*. 10 edition, 1990.

[52] ASM International. *ASM Handbook Volume 02: Properties and Selection: Irons, Steels, and High-Performance Alloys*. 10 edition, 1990.

[53] Eduardo Marques, Alexandre Pereira, and João Ribeiro. Thermal evaluation of MAG/TIG welding using numerical extension tool. *International Journal of Applied Science and Engineering*, 2021.

[54] K. Sunil Kumar Reddy, M. Kannan, R. Karthikeyan, Althati Sripad, and P.K. Jain. Investigation of thermal and mechanical properties of Al7020/SiC/graphite hybrid metal matrix composites. *Metals MDPI*, 2020.

[55] David Bombac, Peter Cvahte, Martin Balog, Goran Kugler, and Milan Tercelj. In-Depth Comparison of An Industrially Extruded Powder and Ingot Al Alloys. *Metals MDPI*, 2020.

[56] Hailin He, Youping Yi, Jindong Cui, and Shiquan Huang. Hot deformation characteristics and processing parameter optimization of 2219 Al alloy using constitutive equation and processing map. *Vacuum*, 2018.

[57] R.K. Gupta, V. Anil Kumar, A. Sarath Krishnan, and J. Niteshraj. Hot deformation behavior of aluminum alloys AA7010 and AA7075. *Journal of Materials Engineering and Performance*, 2019.

[58] Sumit Ghosh, Mahesh Chandra Somani, Daria Setman, and Suhrit Mula. Hot Deformation Characteristic and Strain Dependent Constitutive Flow Stress Modelling of Ti + Nb Stabilized Interstitial Free Steel. *Metals and Materials International*, 2020.

[59] Xianjun Pei and Pingsha Dong. Modeling of banded structure in friction stir weld in strain rate-hardening materials of Zener–Hollomon type. *Journal of Strain Analysis*, 2015.

[60] C.M. Sellars and W.J. McG. Tegart. Hot workability. *International Metallurgical Reviews*, 1972.

[61] Jordan Tsui. Experimental studies and asymptotic scaling for the development of engineering tools to predict coupled heat transfer and plastic deformation in Friction Stir Welding (FSW). *University of Alberta*, 2016.

[62] Benjamin Vergara. Modelamiento Acomplado Termico y de Deformacion en Soldadura por Friccion-Agitacion. *Universidad de Chile*, 2017.

[63] S. Benavides, Y. Li, L.E. Murr, D. Brown, , and J.C. McClure. Low-temperature friction-stir welding of 2024 aluminum. *Scripta Materialia*, 1999.

[64] Ho-Sung Lee, Jong-Hoon Yoon, Joon-Tae Yoo, and Kookil No. Friction Stir Welding Process of Aluminum-Lithium Alloy 2195. *Procedia Engineering*, 2016.

[65] A. P. Reynolds, W. Tang, Z. Khandkar, J. A. Khan, and K. Lindner. Relationships between weld parameters, hardness distribution and temperature history in alloy 7050 friction stir welds. *Science and Technology of Welding and Joining*, 2005.

[66] Karem Tello. Coupled model of heat transfer and plastic deformation for FSW using scaling analysis. *Colorado School of Mines*.

[67] Y.C. Chen, J.C. Feng, and H.J. Liu. Precipitate evolution in friction stir welding of 2219-T6 aluminum alloys. *Materials Characterization*, 2009.

[68] T.J. Lienert, W.L. Stellwag, and H. Shao. Determination of load, torque, and tool temperatures during friction stir welding of aluminum alloys. 2000.

[69] M. Z. H. Khandkar, J. A. Khan, and A. P. Reynolds. Prediction of temperature distribution and thermal history during friction stir welding: input torque based model. *Science and Technology of Welding and Joining*, 2003.

[70] Mustafa Boz and Adem Kurt. The influence of stirrer geometry on bonding and mechanical properties in friction stir welding process. *Materials and Design*, 2004.

[71] H.N.B. Schmidt, T.L. Dickerson, and J.H. Hattel. Material flow in butt friction stir welds in AA2024-T3. *Acta Materialia*, 2006.

[72] Judy Schneider, Ronald Beshears, and Arthur C. Nunes Jr. Interfacial sticking and slipping in the friction stir welding process. *Materials Science and Engineering A*, 2006.

[73] Yuh J. Chao, X. Qi, and W. Tang. Heat Transfer in Friction Stir Welding—Experimental and Numerical Studies. *Journal of Manufacturing Science and Engineering*, 2003.

[74] Z.W. Chen, T. Pasang, and Y. Qi. Shear flow and formation of nugget zone during friction stir welding of aluminium alloy 5083-O. *Materials Science and Engineering A*, 2008.

[75] R. Nandan, G.G. Roy, and T. Debroy. Numerical Simulation of Three-Dimensional Heat Transfer and Plastic Flow During Friction Stir Welding. *Metallurgical and Materials Transactions A*, 2006.

[76] Wanchuck Woo, Levente Balogh, Tamás Ungár, Hahn Choo, and Zhili Feng. Grain structure and dislocation density measurements in a friction-stir welded aluminum alloy using X-ray peak profile analysis. *Materials Science and Engineering A*, 2008.

[77] P. A. Colegrove and H. R. Shercliff. Development of Trivex friction stir welding tool Part 2 – three-dimensional flow modelling. *Science and Technology of Welding and Joining*, 2004.

[78] X.K. Zhu and Y.J. Chao. Numerical simulation of transient temperature and residual stresses in friction stir welding of 304L stainless steel. *Journal of Materials Processing Technology*, 2004.

[79] T.J. Lienert, W.L. Stellwag, Jr., and L.R. Lehman. Process results for FSW of Ti-6Al-4V. 2006.

[80] Bangcheng Yang, Junhui Yan, Michael A. Sutton, and Anthony P. Reynolds. Banded microstructure in AA2024-T351 and AA2524-T351 aluminum friction stir welds Part I. metallurgical studies. *Materials Science and Engineering*, 2004.

[81] C.M. Chen and R. Kovacevic. Finite element modeling of friction stir welding—thermal and thermomechanical analysis. *International Journal of Machine Tools and Manufacture*, 2003.

[82] H Schmidt and J Hattel. A local model for the thermomechanical conditions in friction stir welding. *Modelling and Simulation in Materials Science and Engineering*, 2005.

[83] H Schmidt and J Hattel. Modelling heat flow around tool probe in friction stir welding. *Science and Technology of Welding and Joining*, 2005.

[84] Dongun Kim, Harsha Badarinarayan, Ji Hoon Kim, Chongmin Kim, Kazutaka Okamoto, R.H. Wagoner, and Kwansoo Chung. Numerical simulation of friction stir butt welding process for AA5083-H18 sheets. *European Journal of Mechanics A/Solids*, 2010.

[85] Muhsin J. J., Moneer H. Tolephih, and Muhammed A. M. Effect of friction stir welding parameters (rotation and transverse) speed on the transient temperature distribution in friction stir welding of AA7020-T53. *ARPN Journal of Engineering and Applied Sciences*, 2012.

[86] S Verma, Meenu, and J P Misra. Study on temperature distribution during Friction Stir Welding of 6082 aluminum alloy. *Materials Today: Proceedings*, 2017.

[87] Cecile Genevois, Damien Fabregue, Alexis Deschamps, and Warren J. Poole. On the coupling between precipitation and plastic deformation in relation with friction stir welding of AA2024 T3 aluminium alloy. *Materials Science and Engineering A*, 2006.

[88] M. Mohammadtaheri, M. Haddad-Sabzevar, M. Mazinani, and E. Bahrami Motlagh. The Effect of Base Metal Conditions on the Final Microstructure and Hardness of 2024 Aluminum Alloy Friction-Stir Welds. *Metallurgical and Materials Transactions B*, 2013.

[89] Rui dong Fu, Zeng qiang Sun, Rui cheng Sun, Ying Li, Hui jie Liu, and Lei Liu. Improvement of weld temperature distribution and mechanical properties of 7050 aluminum alloy butt joints by submerged friction stir welding. *Materials and Design*, 2011.

[90] Kh. A. A. Hassan, P. B. Prangnell, A. F. Norman, D. A. Price, and S. W. Williams. Effect of welding parameters on nugget zone microstructure and properties in high strength aluminium alloy friction stir welds. *Science and Technology of Welding and Joining*, 2003.

[91] S Lu, D L Yang, S Y Xiao, and S J Chen. Three-dimensional investigation on temperature distribution and mechanical properties of AZ31 Mg alloy joint welded by FSW. *Proceedings of the 1st International Joint Symposium on Joining and Welding*, 2013.

[92] Hidetoshi Fujii, Ling Cui, Nobuhiro Tsuji, Masakatsu Maeda, Kazuhiro Nakata, and Kiyoshi Nogi. Friction stir welding of carbon steels. *Materials Science and Engineering A*, 2006.

[93] H.J. Zhang, H.J. Liu, , and L. Yu. Effect of Water Cooling on the Performances of Friction Stir Welding Heat-Affected Zone. *Journal of Materials Engineering and Performance*, 2012.

[94] Z. Zhang, B.L. Xiao, and Z.Y. Ma. Hardness recovery mechanism in the heat-affected zone during long-term natural aging and its influence on the mechanical properties and fracture behavior of friction stir welded 2024 Al–T351 joints. *Acta Materialia*, 2014.

Annexes

A. Nominal Material Composition

Table A.1: Nominal material compositions used in JMatPro.

Material	AA1080	AA2195	AA2198	AA2199	AA2219	AA2524	AA6082
Al	99.33%	92.42%	95.049%	93.38%	93.06%	94.151%	95.35%
Fe	0.409%	0.15%	0.046%	-	-	0.06%	0.5%
Si	0.121%	0.12%	0.03%	-	-	0.04%	1.3%
Cu	0.22%	4.3%	3.2%	2.9%	6.3%	3.84%	0.1%
Mn	0.013%	0.25%	0.005%	0.5%	0.3%	0.56%	1%
Mg	0.019%	0.8%	0.31%	0.4%	-	1.31%	1.2%
Zn	0.037%	-	0.014%	0.9%	-	0.01%	0.2%
Ni	0.085%	-	-	-	-	-	-
Cr	0.044%	-	-	-	-	-	0.25%
Pb	0.026%	-	-	-	-	-	-
Sn	0.05%	-	-	-	-	-	-
Ti	0.021%	-	-	-	0.06%	0.029%	0.1%
Sb	0.03%	-	-	-	-	-	-
Ag	-	0.6%	0.27%	-	-	-	-
Li	-	1.2%	1%	1.8%	-	-	-
Zr	-	0.16%	0.076%	0.12%	0.18%	-	-
V	-	-	-	-	0.1%	-	-

Table A.2: Nominal material compositions used in JMatPro. (Cont.)

Material	AA7010	AA7136	SSA038	SAE1012	SAE1035
Al	89.70%	84.93%	88.29%	-	-
Fe	0.1%	0.15%	-	99.9%	99.62%
Si	0.08%	0.12%	-	-	-
Cu	1.81%	2.5%	1.56%	-	-
Mn	-	0.05%	0.25%	-	-
Mg	2.2%	2.5%	2.14%	-	-
Zn	6%	9.4%	7.11%	-	-
Zr	0.11%	0.2%	0.17%	-	-
Cr	-	0.05%	0.05%	-	-
Sc	-	-	0.38%	-	-
Ti	-	0.1%	0.05%	-	-
C	-	-	-	0.1%	0.38%

B. Constitutive Model Constants

Table B.1: Values of constants for the Zener-Hollomon constitutive model.

Material	A' (s^{-1})	n'	Q (kJ/mol)	σ'_R (MPa)	A (s^{-1})	n
AA1080	6.28×10^{11}	3.97	232	36.8	1.81×10^{15}	11.9
AA2024	2.29×10^{11}	5.46	178	47.7	6.52×10^{14}	11.5
AA2195	2.29×10^{12}	2.38	162	293	1.73×10^{12}	3.54
AA2198	2.29×10^{12}	2.38	162	293	2.93×10^{13}	3.37
AA2199	2.29×10^{12}	2.38	162	293	2.93×10^{13}	3.37
AA2219	1.37×10^{11}	6.65	160	68	1.73×10^{16}	10.08
AA2524	1.37×10^{11}	6.65	160	68	1.64×10^{16}	10.01
AA5059	-	-	173	-	3.84×10^{8}	8.41
AA5083	1.64×10^{10}	2.44	173	34.8	1.78×10^{15}	8.44
AA6061	1.63×10^{13}	5.33	191	60.7	1.72×10^{13}	7.68
AA6082	1.63×10^{13}	5.33	191	60.7	3.28×10^{13}	7.7
AA7010	5.04×10^{19}	0.99	347	11.4	2.23×10^{22}	15.87
AA7020	5.04×10^{19}	0.99	347	11.4	1.91×10^{23}	8.29
AA7050	1.45×10^{10}	3.39	165	32.5	6.48×10^{13}	10.7
AA7075	5.34×10^{8}	3.47	160	33.9	1.74×10^{12}	11.95
AA7136	5.34×10^{8}	3.47	160	33.9	2.13×10^{19}	12.61
SSA038	5.34×10^{8}	3.47	160	33.9	1.63×10^{12}	12.06
IF	5.6×10^{12}	5.8	285	113.6	3.12×10^{14}	6.2
SAE1012	2.36×10^{13}	4.32	350	56.6	6.1×10^{16}	5.92
SAE1018	2.36×10^{13}	4.32	371	56.6	6.95×10^{16}	5.67
SAE1035	2.36×10^{13}	4.32	390	56.6	2.49×10^{17}	6.65
304SS	1.62×10^{16}	4.69	441	119	4.36×10^{18}	5.51
Ti-6Al-4V	3.37×10^{8}	3.39	231	47.9	3.96×10^{14}	4.63
AZ31	-	-	127	-	6.26×10^{12}	7.57

C. Summary of data compiled

The following Tables present the data compiled from the literature for every experiment, simulation or numerical model considered in this work. The data correspond to process parameters, torque and maximum temperature. Units: V (mm/s); a, b and d (mm); $T_{max}(K)$; M (Nm).

Table C.1: Process parameters from de database.

Type	Material	V	RPM	a	b	d	Tmax	M	Ref
Exp	AA2219	1.33	550	4.90	14.00	14.00	665	-	[29]
Exp	AA2219	1.33	600	4.90	14.00	14.00	674	-	[29]
Exp	AA2219	1.67	600	4.90	14.00	14.00	666	-	[29]
Exp	AA2219	1.67	800	3.70	11.25	7.50	693	-	[93]
Exp	AA2219	1.67	800	3.70	11.25	7.50	671	-	[93]
Exp	AA2024	6.77	800	4.00	10.00	5.00	613	-	[94]
Exp	AA2195	3.33	800	3.30	8.00	6.35	783	-	[25]
Exp	AA2199	3.33	800	3.30	8.00	4.00	803	-	[25]
Exp	AA5059	15.00	1723	1.50	4.50	4.00	668	7	[61]
Exp	AA5059	15.00	1225	2.00	6.00	5.30	718	6	[61]
Exp	AA5059	15.00	1225	2.50	7.50	6.70	762	10	[61]
Exp	AA5059	15.00	1225	2.00	4.50	5.30	708	10	[61]
Exp	AA5059	15.00	1225	2.00	7.50	5.30	761	8	[61]
Exp	AA5059	15.00	1723	1.50	4.50	4.00	695	3	[61]
Exp	AA5059	15.00	1225	2.00	6.00	5.30	727	6	[61]
Exp	AA5059	15.00	1225	2.50	7.50	6.70	731	12	[61]
Exp	AA5059	15.00	1225	2.00	4.50	5.30	712	7	[61]
Exp	AA5059	15.00	1225	2.00	7.50	5.30	748	7	[61]

Table C.2: Process parameters from de database. (Cont.)

Type	Material	V	RPM	a	b	d	Tmax	M	Ref
Exp	AA2024	2.00	400	3.00	9.00	3.00	673	40	[43]
Exp	AA2024	2.00	400	3.00	9.00	3.00	-	-	[71]
Exp	AA2195	1.70	180	5.80	15.25	25.00	-	-	[26]
Exp	AA2195	2.50	200	6.35	15.25	8.20	-	-	[72]
Exp	AA2195	2.36	240	5.00	12.70	8.10	698	-	[73]
Exp	AA2195	3.32	240	5.00	12.70	8.10	678	-	[73]
Exp	AA5083	1.69	250	7.60	21.00	25.40	803	295	[10]
Exp	AA5083	2.12	250	7.60	21.00	25.40	818	326	[10]
Exp	AA5083	2.54	250	7.60	21.00	25.40	848	358	[10]
Exp	AA5083	2.00	760	3.00	10.00	8.00	-	-	[74]
Sim	AA5083	1.27	123	5.00	14.30	9.50	-	181	[15]
Sim	AA5083	1.27	163	5.00	14.30	9.50	-	152	[15]
Sim	AA5083	1.27	202	5.00	14.30	9.50	-	128	[15]
Sim	AA5083	1.27	245	5.00	14.30	9.50	-	108	[15]
Sim	AA5083	1.27	291	5.00	14.30	9.50	-	94	[15]
Sim	AA5083	1.27	361	5.00	14.30	9.50	-	79	[15]
Sim	AA5083	1.27	415	5.00	14.30	9.50	-	70	[15]
Sim	AA5083	1.27	487	5.00	14.30	9.50	-	64	[15]
Sim	AA5083	1.27	596	5.00	14.30	9.50	-	50	[15]
Sim	AA5083	1.27	703	5.00	14.30	9.50	-	40	[15]
Sim	AA5083	1.27	809	5.00	14.30	9.50	-	35	[15]
Exp	AA5083	4.66	815	3.15	9.53	6.35	623	24	[68]
Num	AA6061	2.40	390	5.00	12.70	8.13	683	-	[69]
Exp	AA6061	1.59	636	6.00	25.00	12.70	820	-	[11]
Exp	AA6061	3.33	500	6.00	9.00	12.70	770	-	[11]
Exp	AA6061	2.00	400	6.00	9.00	12.70	773	-	[11]
Exp	AA6061	2.22	344	6.00	12.00	12.70	766	-	[11]
Exp	AA6061	2.37	390	6.00	25.00	12.70	755	-	[11]

Table C.3: Process parameters from de database. (Cont.)

Type	Material	V	RPM	a	b	d	Tmax	M	Ref
Num	AA6061	0.50	200	6.00	25.00	12.70	742	-	[11]
Num	AA6061	1.00	200	6.00	25.00	12.70	736	-	[11]
Num	AA6061	1.50	200	6.00	25.00	12.70	729	-	[11]
Num	AA6061	1.50	400	6.00	25.00	12.70	791	-	[11]
Num	AA6061	1.00	400	6.00	25.00	12.70	795	-	[11]
Num	AA6061	0.50	400	6.00	25.00	12.70	799	-	[11]
Num	AA6061	0.50	600	6.00	25.00	12.70	820	-	[11]
Num	AA6061	1.00	600	6.00	25.00	12.70	818	-	[11]
Num	AA6061	1.50	600	6.00	25.00	12.70	814	-	[11]
Exp	AA6061	1.60	600	6.00	25.00	12.70	790	-	[75]
Exp	AA6061	1.60	400	6.00	25.00	12.70	745	-	[75]
Exp	AA6061	1.60	200	6.00	25.00	12.70	685	-	[75]
Sim	AA6061	1.60	344	6.00	25.00	12.70	790	-	[75]
Sim	AA6061	0.50	200	6.00	25.00	12.70	700	-	[75]
Sim	AA6061	1.00	200	6.00	25.00	12.70	694	-	[75]
Sim	AA6061	1.50	200	6.00	25.00	12.70	688	-	[75]
Sim	AA6061	0.50	400	6.00	25.00	12.70	763	-	[75]
Sim	AA6061	1.00	400	6.00	25.00	12.70	756	-	[75]
Sim	AA6061	1.50	400	6.00	25.00	12.70	750	-	[75]
Sim	AA6061	0.50	600	6.00	25.00	12.70	807	-	[75]
Sim	AA6061	1.00	600	6.00	25.00	12.70	802	-	[75]
Sim	AA6061	1.50	600	6.00	25.00	12.70	797	-	[75]
Exp	AA6061	2.36	390	5.00	12.70	8.13	665	84	[69]
Exp	AA6061	4.66	1182	2.81	9.53	6.35	625	31	[68]
Sim	AA6061	1.59	637	6.00	50.00	12.70	-	-	[37]
Exp	AA6061	3.00	1000	3.15	9.50	6.30	-	-	[27]
Exp	AA6061	1.28	240	5.00	12.70	8.13	-	-	[12]
Exp	AA6061	2.36	240	5.00	12.70	8.13	-	-	[12]
Exp	AA6061	3.32	240	5.00	12.70	8.13	-	-	[12]
Exp	AA6061	2.36	290	5.00	12.70	8.13	-	-	[12]
Exp	AA6061	2.36	340	5.00	12.70	8.13	-	-	[12]
Exp	AA6061	1.28	390	5.00	12.70	8.13	-	-	[12]
Exp	AA6061	2.36	390	5.00	12.70	8.13	-	-	[12]
Exp	AA6061	3.32	390	5.00	12.70	8.13	-	-	[12]
Exp	AA6061	2.36	720	5.00	12.70	8.13	-	-	[12]
Exp	AA6061	2.36	800	5.00	12.70	8.13	-	-	[12]
Exp	AA6061	0.50	400	3.25	12.90	6.30	-	-	[13]
Exp	AA6061	1.50	400	3.25	12.90	6.30	-	-	[13]
Exp	AA6061	2.50	400	3.25	12.90	6.30	-	-	[13]

Table C.4: Process parameters from de database. (Cont.)

Type	Material	V	RPM	a	b	d	Tmax	M	Ref
Exp	AA6061	3.50	400	3.25	12.90	6.30	-	-	[13]
Exp	AA6061	0.42	156	3.18	12.70	6.35	-	-	[76]
Exp	AA6061	3.39	650	4.00	12.70	9.53	820	-	[41]
Sim	AA6061	3.39	650	4.00	12.70	9.53	768	-	[41]
Sim	AA6061	3.39	650	4.00	12.70	9.53	781	-	[41]
Sim	AA6061	3.39	650	4.00	12.70	9.53	803	-	[41]
Sim	AA7050	0.85	91	3.55	10.15	6.40	506	-	[14]
Sim	AA7050	0.85	182	3.50	10.15	6.40	589	-	[14]
Sim	AA7050	2.54	272	3.55	10.15	6.40	638	-	[14]
Sim	AA7050	3.81	387	3.55	10.15	6.40	663	-	[14]
Exp	AA7050	0.84	179	3.55	10.15	6.40	-	73	[14]
Exp	AA7050	1.25	129	3.55	10.20	6.40	-	118	[14]
Exp	AA7050	1.68	173	3.55	10.20	6.40	-	172	[14]
Exp	AA7050	2.52	261	3.55	10.20	6.40	-	78	[14]
Exp	AA7050	2.95	305	3.55	10.20	6.40	-	69	[14]
Exp	AA7050	3.80	393	3.55	10.20	6.40	-	64	[14]
Exp	AA7050	4.25	911	3.55	10.20	6.40	-	27	[14]
Exp	AA7050	1.25	179	3.55	10.15	6.40	-	80	[14]
Exp	AA7050	1.68	239	3.55	10.20	6.40	-	66	[14]
Exp	AA7050	2.50	357	3.55	10.20	6.40	-	53	[14]
Exp	AA7050	3.75	536	3.55	10.15	6.40	-	42	[14]
Exp	AA7050	5.10	729	3.55	10.15	6.40	-	32	[14]
Exp	AA7050	0.80	86	3.55	10.15	6.40	-	106	[14]
Exp	AA7050	1.26	131	3.55	10.15	6.40	-	101	[14]
Exp	AA7050	1.70	182	3.55	10.20	6.40	-	86	[14]
Exp	AA7050	2.50	262	3.55	10.15	6.40	-	74	[14]
Exp	AA7050	2.95	305	3.55	10.20	6.40	-	63	[14]
Exp	AA7050	3.75	402	3.55	10.15	6.40	-	55	[14]
Num	AA7050	0.90	182	3.55	10.15	6.40	592	-	[65]
Num	AA7050	1.70	364	3.55	10.15	6.40	671	-	[65]
Num	AA7050	2.50	544	3.55	10.15	6.40	661	-	[65]
Num	AA7050	3.80	814	3.55	10.15	6.40	703	-	[65]
Exp	AA7050	1.27	60	5.00	14.30	9.50	-	305	[15]
Exp	AA7050	1.27	85	5.00	14.30	9.50	-	275	[15]
Exp	AA7050	1.27	110	5.00	14.30	9.50	-	205	[15]
Exp	AA7050	1.27	145	5.00	14.30	9.50	-	155	[15]
Exp	AA7050	1.27	180	5.00	14.30	9.50	-	130	[15]
Exp	AA7050	1.27	215	5.00	14.30	9.50	-	90	[15]
Exp	AA7050	1.27	250	5.00	14.30	9.50	-	75	[15]

Table C.5: Process parameters from de database. (Cont.)

Type	Material	V	RPM	a	b	d	Tmax	M	Ref
Exp	AA7050	1.27	290	5.00	14.30	9.50	-	70	[15]
Exp	AA7050	1.27	400	5.00	14.30	9.50	-	60	[15]
Exp	AA7050	1.27	520	5.00	14.30	9.50	-	55	[15]
Exp	AA7050	1.27	550	5.00	14.30	9.50	-	50	[15]
Exp	AA7075	3.00	302	8.25	24.75	16.00	803	199	[16]
Exp	AA7075	4.00	302	8.25	24.75	16.00	813	221	[16]
Exp	AA7075	5.00	302	8.25	24.75	16.00	823	245	[16]
Exp	AA7075	2.55	255	8.25	24.75	16.00	808	224	[16]
Exp	AA7075	3.43	255	8.25	24.75	16.00	813	250	[16]
Exp	AA7075	4.25	255	8.25	24.75	16.00	803	271	[16]
Exp	AA7075	5.10	255	8.25	24.75	16.00	798	292	[16]
Exp	AA7075	3.67	220	8.25	24.75	16.00	803	342	[16]
Exp	AA7075	4.40	220	8.25	24.75	16.00	808	344	[16]
Exp	AA7075	5.13	220	8.25	24.75	16.00	798	356	[16]
Exp	AA7075	5.95	220	8.25	24.75	16.00	-	385	[16]
Exp	AA7075	3.17	190	8.25	24.75	16.00	-	311	[16]
Exp	AA7075	6.12	457	6.35	19.05	6.35	-	-	[16]
Exp	AA7075	7.62	457	6.35	19.05	6.35	773	95	[16]
Exp	AA7075	5.25	394	6.35	19.05	6.35	793	-	[16]
Exp	AA7075	6.57	394	6.35	19.05	6.35	758	119	[16]
Exp	AA7075	7.87	394	6.35	19.05	6.35	738	130	[16]
Exp	AA7075	7.62	457	4.00	11.50	6.35	773	-	[77]
Exp	AA7075	4.66	1182	2.81	9.53	6.35	604	59	[68]
Num	304SS	1.69	300	3.17	9.53	3.18	570	-	[38]
Exp	304SS	1.69	300	3.17	9.53	3.18	1243	-	[78]
Exp	304SS	1.69	500	3.17	9.53	3.18	-	-	[78]
Exp	304SS	1.69	300	3.20	9.50	3.20	1430	-	[11]
Num	304SS	0.85	400	3.20	9.50	3.20	1412	-	[11]
Num	304SS	0.85	500	3.20	9.50	3.20	1518	-	[11]
Num	304SS	0.85	300	3.20	9.50	3.20	1316	-	[11]
Num	304SS	1.70	400	3.20	9.50	3.20	1313	-	[11]
Num	304SS	1.70	500	3.20	9.50	3.20	1385	-	[11]
Num	304SS	1.70	300	3.20	9.50	3.20	1241	-	[11]
Num	304SS	2.55	300	3.20	9.50	3.20	1200	-	[11]
Num	304SS	2.55	400	3.20	9.50	3.20	1256	-	[11]
Num	304SS	2.55	500	3.20	9.50	3.20	1314	-	[11]
Num	SAE1018	0.40	550	3.95	9.53	6.35	1428	-	[11]
Num	SAE1018	0.40	650	3.95	9.53	6.35	1506	-	[11]
Num	SAE1018	0.40	450	3.95	9.53	6.35	1349	-	[11]

Table C.6: Process parameters from de database. (Cont.)

Type	Material	V	RPM	a	b	d	Tmax	M	Ref
Num	SAE1018	0.80	450	3.95	9.53	6.35	1286	-	[11]
Num	SAE1018	1.20	450	3.95	9.53	6.35	1236	-	[11]
Num	SAE1018	0.80	550	3.95	9.53	6.35	1359	-	[11]
Num	SAE1018	1.20	550	3.95	9.53	6.35	1301	-	[11]
Num	SAE1018	0.80	650	3.95	9.53	6.35	1423	-	[11]
Num	SAE1018	1.20	650	3.95	9.53	6.35	1361	-	[11]
Exp	SAE1018	0.40	450	3.95	9.53	6.35	1273	-	[11]
Exp	SAE1018	0.42	450	4.00	9.50	6.35	938	55	[28]
Exp	Ti-6Al-4V	1.60	275	3.95	9.50	7.20	1143	-	[79]
Sim	AA2024	4.45	360	4.00	12.00	6.40	788	-	[22]
Sim	AA2024	3.29	360	4.00	12.00	6.40	763	-	[22]
Sim	AA2024	1.28	215	4.00	12.00	6.40	603	-	[22]
Sim	AA6061	2.33	500	3.00	12.00	6.00	653	-	[81]
Sim	AA6061	5.83	500	3.00	12.00	6.00	764	-	[81]
Exp	AA2024	2.00	400	3.00	9.00	3.00	773	-	[82]
Exp	AA2024	2.00	400	3.00	9.00	3.00	708	-	[83]
Exp	AA5083	1.67	1000	2.00	5.00	1.64	798	-	[84]
Sim	AA5083	1.67	1000	2.00	5.00	1.64	798	-	[84]
Exp	AA5083	5.00	1000	2.00	5.00	1.64	733	-	[84]
Sim	AA5083	5.00	1000	2.00	5.00	1.64	740	-	[84]
Exp	AA5083	2.50	1500	2.00	5.00	1.64	803	-	[84]
Sim	AA5083	2.50	1500	2.00	5.00	1.64	813	-	[84]
Num	SAE1018	0.42	450	3.95	9.50	6.35	1463	-	[42]
Sim	SAE1018	0.02	350	3.95	9.50	6.35	1170	69	[42]
Sim	SAE1018	0.06	350	3.95	9.50	6.35	1138	71	[42]
Sim	SAE1018	0.10	350	3.95	9.50	6.35	1107	73	[42]
Sim	SAE1018	0.14	350	3.95	9.50	6.35	1061	76	[42]
Sim	SAE1018	0.02	450	3.95	9.50	6.35	1229	55	[42]
Sim	SAE1018	0.06	450	3.95	9.50	6.35	1168	58	[42]
Sim	SAE1018	0.10	450	3.95	9.50	6.35	1140	59	[42]
Sim	SAE1018	0.14	450	3.95	9.50	6.35	1097	61	[42]
Sim	SAE1018	0.02	550	3.95	9.50	6.35	1293	46	[42]
Sim	SAE1018	0.06	550	3.95	9.50	6.35	1211	48	[42]
Sim	SAE1018	0.10	550	3.95	9.50	6.35	1170	50	[42]
Sim	SAE1018	0.14	550	3.95	9.50	6.35	1128	51	[42]
Sim	SAE1018	0.02	650	3.95	9.50	6.35	1351	39	[42]
Sim	SAE1018	0.06	650	3.95	9.50	6.35	1254	41	[42]
Sim	SAE1018	0.10	650	3.95	9.50	6.35	1193	43	[42]
Sim	SAE1018	0.14	650	3.95	9.50	6.35	1152	44	[42]

Table C.7: Process parameters from de database. (Cont.)

Type	Material	V	RPM	a	b	d	Tmax	M	Ref
Exp	AA6082	1.92	880	3.00	9.50	5.00	513	-	[31]
Exp	AA2195	5.00	600	3.00	9.50	5.00	480	-	[64]
Exp	AA6061	2.00	300	3.00	10.00	6.40	698	-	[17]
Exp	AA6061	2.00	400	3.00	10.00	6.40	723	-	[17]
Exp	AA6061	2.00	650	3.00	10.00	6.40	728	-	[17]
Exp	AA6061	2.00	1000	3.00	10.00	6.40	748	-	[17]
Exp	AA1080	3.33	1000	4.50	10.00	5.00	610	-	[70]
Sim	AA2024	1.33	600	2.13	7.50	5.90	756	16	[18]
Sim	AA2024	1.33	800	2.13	7.50	5.90	818	12	[18]
Sim	AA2024	1.33	1000	2.13	7.50	5.90	843	12	[18]
Exp	AA7020	0.67	1400	3.00	9.00	5.00	629	-	[85]
Sim	AA7020	0.67	1400	3.00	9.00	5.00	642	-	[85]
Sim	AA7020	0.67	900	3.00	9.00	5.00	615	-	[85]
Sim	AA7020	0.27	1400	3.00	9.00	5.00	680	-	[85]
Exp	AA6082	20.00	500	3.00	10.00	6.35	532	-	[86]
Exp	AA6082	20.00	500	3.00	10.00	6.35	521	-	[86]
Exp	AA6082	20.00	500	3.00	10.00	6.35	528	-	[86]
Exp	AA6082	20.00	500	3.00	10.00	6.35	557	-	[86]
Exp	AA6082	20.00	500	3.00	10.00	6.35	534	-	[86]
Exp	AA7075	0.83	500	3.00	9.50	5.00	658	-	[33]
Exp	AA7075	0.83	500	3.00	9.50	5.00	638	-	[33]
Exp	AA7075	0.83	500	3.00	9.50	5.00	627	-	[33]
Exp	Ti-6Al-4V	1.67	200	5.00	12.50	12.00	1277	-	[19]
Exp	Ti-6Al-4V	1.67	300	5.00	12.50	12.00	1373	-	[19]
Exp	Ti-6Al-4V	1.67	400	5.00	12.50	12.00	1422	-	[19]
Exp	Ti-6Al-4V	0.83	300	5.00	12.50	12.00	1385	-	[19]
Exp	Ti-6Al-4V	2.50	300	5.00	12.50	12.00	1361	-	[19]
Exp	SSA038	2.10	225	4.50	8.90	6.35	619	-	[20]
Exp	SSA038	2.10	250	4.50	8.90	6.35	623	-	[20]
Exp	SSA038	2.10	300	4.50	8.90	6.35	645	-	[20]
Exp	SSA038	2.10	400	4.50	8.90	6.35	663	-	[20]
Sim	SSA038	2.10	225	4.50	8.90	6.35	586	-	[20]
Sim	SSA038	2.10	250	4.50	8.90	6.35	593	-	[20]
Sim	SSA038	2.10	300	4.50	8.90	6.35	638	-	[20]
Sim	SSA038	2.10	400	4.50	8.90	6.35	664	-	[20]
Exp	AA2024	1.33	400	1.50	4.00	1.60	608	-	[21]
Exp	AA2024	3.33	700	1.50	4.00	1.60	673	-	[21]
Exp	AA2024	16.67	1500	1.50	4.00	1.60	708	-	[21]
Exp	AA2024	2.00	1200	1.50	4.00	1.60	728	-	[21]

Table C.8: Process parameters from de database. (Cont.)

Type	Material	V	RPM	a	b	d	Tmax	M	Ref
Exp	AA2024	1.00	650	3.25	9.50	6.50	603	-	[63]
Exp	AA2024	1.00	650	3.25	9.50	6.50	413	-	[63]
Exp	AA2024	2.00	850	3.00	8.00	6.00	613	-	[87]
Exp	AA2024	1.28	215	4.00	10.00	6.40	598	95	[80]
Exp	AA2024	3.29	360	4.00	10.00	6.40	753	77	[80]
Exp	AA2024	4.45	360	4.00	10.00	6.40	788	87	[80]
Exp	AA2524	0.85	120	4.00	10.00	6.40	578	124	[80]
Exp	AA2524	2.11	300	4.00	10.00	6.40	653	66	[80]
Exp	AA2524	3.38	480	4.00	10.00	6.40	673	46	[80]
Exp	AA2024	0.37	1547	4.00	8.00	4.00	725	-	[88]
Exp	AA2024	0.37	1547	4.00	8.00	4.00	706	-	[88]
Exp	AA2024	1.25	468	4.00	8.00	6.35	754	-	[23]
Exp	AA2024	2.57	215	4.00	8.00	6.35	523	-	[23]
Exp	AA2024	2.57	468	4.00	8.00	6.35	548	-	[23]
Exp	AA2024	1.58	350	4.00	8.00	6.35	573	-	[23]
Exp	AA2024	1.25	215	4.00	8.00	6.35	545	-	[23]
Exp	AA2024	1.25	468	4.00	8.00	6.35	603	-	[23]
Exp	AA2198	0.70	400	2.00	5.50	3.20	525	13	[30]
Exp	AA2198	0.70	600	2.00	5.50	3.20	540	11	[30]
Exp	AA2198	0.70	800	2.00	5.50	3.20	575	9	[30]
Exp	AA2198	0.70	1000	2.00	5.50	3.20	603	8	[30]
Exp	AA7050	3.40	250	3.50	9.00	6.35	683	-	[24]
Exp	AA7050	6.80	650	3.50	9.00	6.35	743	-	[24]
Exp	AA7050	10.20	1000	3.50	9.00	6.35	773	-	[24]
Exp	AA7050	1.67	800	3.10	6.00	5.50	643	-	[89]
Exp	AA7010	1.58	180	5.00	10.00	6.35	674	-	[90]
Exp	AA7010	1.58	350	5.00	10.00	6.35	749	-	[90]
Exp	AA7010	0.98	280	5.00	10.00	6.35	740	-	[90]
Exp	AA7136	2.10	250	4.50	8.90	6.35	587	-	[39]
Exp	AA7136	2.10	350	4.50	8.90	6.35	688	-	[39]
Exp	AZ31	0.83	1500	2.00	8.00	4.00	722	-	[91]
Exp	IF Steel	6.67	400	2.00	6.00	4.00	916	-	[92]
Exp	IF Steel	1.67	400	2.00	6.00	1.20	1112	-	[92]
Exp	SAE1012	1.67	400	2.00	6.00	1.20	1063	-	[92]
Exp	SAE1012	6.67	400	2.00	6.00	1.20	913	-	[92]
Exp	SAE1035	1.67	400	2.00	6.00	1.20	1146	-	[92]
Exp	SAE1035	3.33	400	2.00	6.00	1.20	1014	-	[92]
Exp	SAE1035	6.67	400	2.00	6.00	1.20	926	-	[92]
Exp	AA2219	3.33	800	2.40	7.00	5.00	740	-	[67]